

8-5-2021

## Hydrodynamic Characteristics of the Shortfin Mako Shark (*Isurus oxyrinchus*) for Two Caudal Fin Morphologies

Matthew C. Rodriguez  
Coastal Carolina University

Follow this and additional works at: <https://digitalcommons.coastal.edu/etd>



Part of the [Biophysics Commons](#)

---

### Recommended Citation

Rodriguez, Matthew C., "Hydrodynamic Characteristics of the Shortfin Mako Shark (*Isurus oxyrinchus*) for Two Caudal Fin Morphologies" (2021). *Electronic Theses and Dissertations*. 136.  
<https://digitalcommons.coastal.edu/etd/136>

This Thesis is brought to you for free and open access by the College of Graduate and Continuing Studies at CCU Digital Commons. It has been accepted for inclusion in Electronic Theses and Dissertations by an authorized administrator of CCU Digital Commons. For more information, please contact [commons@coastal.edu](mailto:commons@coastal.edu).



Hydrodynamic Characteristics of the Shortfin Mako Shark (*Isurus oxyrinchus*) for Two  
Caudal Fin Morphologies

By

Matt Rodriguez

---

Submitted in Partial Fulfillment of the  
Requirements for the Degree of Master of Science in  
Coastal Marine and Wetland Studies in the  
School of the Coastal Environment  
Coastal Carolina University  
Summer 2021

---

Dr. Erin E. Hackett, Major Professor

---

Dr. Roi Gurka, Major Professor

---

Dr. Daniel Abel, Committee Member

---

Dr. Richard Viso, CMWS Coordinator

---

Dr. Michael H. Roberts, Dean



## Acknowledgements

I will never be able to properly thank my advisors Dr. Erin Hackett and Dr. Roi Gurka for everything they have done for me throughout this entire process. I came to this lab knowing next to nothing about fluid dynamics or, never having done any coding, and had never even heard of PIV. Thanks to their patience and knowledge I have earned this degree. Having been given such an opportunity has meant the world to me, and although I'm sure it felt like pulling teeth at times, thank you. Thank you Erin for giving me the original opportunity to work here. I'm lucky, I know that I am for having had the opportunity to work with and learn from you. Thank you Roi for lending me your expertise and truly incredible breadth of knowledge on the topic of fluid dynamics. I am honored to have been your student. I would also like to thank Dr. Dan Abel for serving on my committee. Being able to work with and learn about sharks with and from you has meant the world to me. I realize how lucky I have been in that respect. Lastly, thank you Coastal Carolina University for providing the funding for this study.

To everyone in the EFL, how do I say thank you enough? Thank you Danny for being one of my best friends at Coastal. Thank you Doug for helping me learn MATLAB in the beginning and being a great gym buddy. Thank you Vivian for helping me learn through your experience. Thank you Mat for teaching me how to operate the flume and run PIV. Thank you Kiki for helping me learn MATLAB as well, and for proofreading some of my documents. Thank you Anup and Asif for also helping with my coding and helping to teach me fluid dynamics. Sarah, thank you for all of your help. I would like to extend a special thank you to Tim Hesford, without his work on our shark models, this research would have taken much more time to complete. Lastly, I would like to thank my parents, whose love and support throughout my education has continuously motivate me to pursue this advanced degree.

## Abstract

Many aquatic organisms locomote using highly efficient oscillatory motions. Within elasmobranchs, the Shortfin Mako is considered the most hydromechanically efficient species. They have evolved numerous morphological adaptations to enhance their hydromechanical efficiency. For this study, we considered the lunate caudal fin and thunniform oscillations Shortfin Makos employ to propel themselves. Most elasmobranchs have a heterocercal caudal fin paired with carangiform oscillations. This study investigated the hydrodynamics of the Shortfin Mako, using a flexible scale model with a robust oscillating caudal fin that emulates this species' natural thunniform body motions. Here, the Shortfin Mako's lunate caudal fin was replaced with the heterocercal caudal fin common to most other sharks; a comparison between the wake characteristics of two morphologies was performed to help understand the effect caudal fin morphology has on hydrodynamics when paired with thunniform oscillations. Experiments were conducted in a recirculating water flume using PIV to measure the velocity field in two orthogonal planes: one in the streamwise-spanwise plane and one in the streamwise-normal plane of the near wake of each oscillating caudal fin morphology. The velocity fields were used to estimate the sectional drag formed during steady forward swimming as well as the near-wake turbulence characteristics. Results indicate that the different morphologies generated similar wake characteristics except for fluctuating vorticity, which could imply that the thunniform propulsion mechanism is a bigger factor in the hydrodynamic performance of the Shortfin Mako than caudal fin morphology, and that for the characteristics studied, caudal fin morphology primarily affects the amount of rotational kinetic energy imparted to the wake.

## Table of Contents

<b>1.0 Introduction</b> .....	1
<b>2.0 Background</b> .....	3
2.1 Fish Propulsion.....	3
2.2 Shark Propulsion .....	7
2.3 Lamnids and Scombrids .....	8
2.4 Caudal Fin Morphology.....	9
2.5 Shortfin Mako Shark .....	13
<b>3.0 Research Objectives</b> .....	20
<b>4.0 Methods</b> .....	21
4.1 Shortfin Mako Model.....	21
4.2 Facility .....	23
4.3 Particle Image Velocimetry .....	24
4.3.1 PIV Image Analysis .....	25
4.4 Experiments .....	27
4.4.1 Reynolds Number.....	27
4.4.2 Strouhal Number.....	28
4.5 Data Analysis.....	28
4.5.1 Vorticity.....	29
4.5.2 Reynolds Shear Stresses.....	29
4.5.3 Turbulent Kinetic Energy.....	30
4.5.4 Spectra .....	31
4.5.5 Hydrodynamic Forces .....	32
<b>5.0 Results</b> .....	42
5.1 Wake Characteristics.....	42
5.1.1 Spectra .....	45
5.2 Hydrodynamic Forces .....	46
<b>6.0 Summary and Conclusions</b> .....	58
<b>7.0 References</b> .....	61

### List of Tables

Table 1: Summary of conducted experiments and associated parameters. All the experiments were performed in a water depth of 0.38m and flow speed of ~0.2m/s.....	33
Table 2: Measured PIV planes and morphologies along with associated fin parameters phase, local $Re$ , free stream velocity, and, $C_D$ . Results from previous experiments are also listed in the table - Tamura and Takagi, (2008) <sup>1*</sup> , Takagi et al., (2013) <sup>2*</sup> , Sagong et al., (2013) <sup>3*</sup> .....	49

## List of Figures

Figure 1: Vortex street behind a cylinder with flow moving from left to right, red indicating positive vorticity, and blue indicating negative vorticity (image provided courtesy of Krishnamoorthy Krishnan). .....	15
Figure 2: Depiction of the 4 most common fish swimming modes, with thunniform swimming being the focus of this study. Fish Physiology, (1978). .....	16
Figure 3: Three-dimensional wake structure of a tuna showing the sickle-shaped vortices. From Xia et al., (2015). .....	17
Figure 4: Dual ring vortex structure in the wake of a heterocercal caudal fin. From Fish and Lauder, (2006). .....	18
Figure 5: Image of a shortfin Mako shark with its caudal fin enlarged to show the hypochordal lobe, epichordal lobe, chord, and span. Source: CSIRO National Fish Collection. License: CC-BY-Attribution. ....	19
Figure 6: Figure 6: Shortfin Mako 3D drawing (TurboSquid.com) used to create the mold. ....	34
Figure 7: Schematic of the Shortfin Mako mold, i.e., the negative of the Shortfin Mako drawing in Figure 6, where the vertical black lines indicate the different sections of the mold that were printed separately. ....	35
Figure 8: Line drawing of the mold of the heterocercal caudal fin morphology investigated in this experiment, modeled after a Blacktip Shark ( <i>Carcharhinus limbatus</i> ). .....	36
Figure 9: Image of the silicone shark model with the lunate caudal fin morphology attached. a. Protective housing surrounding the servo motor. b. Support plate which anchors the model. c. Swim plate which allows the caudal fin to oscillate. ....	37
Figure 10: Isometric rendering of the flume. Courtesy of Jerry Quick. ....	38

Figure 11: The Shortfin Mako model positioned in the flume with the laser illuminating the streamwise-spanwise (x, y) plane behind the fork of the lunate caudal fin..... 39

Figure 12: Schematic of the cross-correlation process used in PIV analysis. From Wieneke, (2017)..... 40

Figure 13: Image showing the phases used during this experiment. The left and right phases were used for the streamwise-spanwise plane, and the mid phase for the streamwise-normal plane. Based-on image from Ay et al., (2018). ..... 41

Figure 14: Contours of the left and mid phase of the streamwise velocity components for each morphology. Subplots a, b, and c show the upper, fork, and span measurement planes for the lunate morphology, and subplots d, e, and f show the upper, fork and span PIV measurement planes of the heterocercal morphology. The panel at the top shows the PIV measurement plane locations for reference, labelled by their corresponding subfigure letter. .... 50

Figure 15: Contours of the left and mid phase normal and spanwise vorticity components for each morphology. Subplots a, b, and c show the upper, fork, and streamwise PIV measurement planes of the lunate morphology, and subplots d, e, and f show the upper, fork, and span PIV measurement planes of the heterocercal morphology. The panel at the tops shows the PIV measurement plane locations for reference, labelled by their corresponding subfigure letter... 51

Figure 16: Contours of the left and mid phase Reynolds shear stresses for each morphology. Subplots a, b, and c show the upper, fork, and span PIV measurement planes of the lunate morphology, and subplots d, e, and f show the upper, fork, and span PIV measurement planes of the hetero morphology. The panel at the top shows the PIV measurement plane locations for reference, labelled by their corresponding subfigure letter. .... 52

Figure 17: Phase averaged TKE for the left and mid phase for each morphology. Subplots a, b, and c show the upper, fork, and span PIV measurement planes of the lunate morphology, and

subplots d, e, and f show the upper, fork, and span PIV measurement planes of the heterocercal morphology. The panel at the top shows the PIV measurement plane locations for reference, labelled by their corresponding subfigure letter. .... 53

Figure 18: Fluctuating streamwise velocity spectra in the streamwise, spanwise, and normal directions from data measured at the upper and fork PIV measurement planes respectively. Subplot c shows spectra computed along the streamwise and normal directions for data measured at the span PIV measurement plane. The green line represents the  $k^{-5/3}$  power law for turbulence in the inertial range. .... 54

Figure 19: Phase averaged fluctuating normal and spanwise vorticity spectra along the streamwise, normal, and spanwise directions. Subplots a and b show fluctuating normal vorticity spectra computed along the streamwise and spanwise directions from data measured at the upper and fork PIV measurement planes respectively. Subplot c shows fluctuating spanwise vorticity spectra computed along the streamwise and normal directions for data measured at the span PIV measurement plane. .... 55

Figure 20: Phase-averaged momentum deficit (a, b) spanwise and (c) normal profiles in the wake behind an oscillating Shortfin Mako model. Velocities are phase-averaged and averaged over the streamwise direction between the two vertical black lines shown in Figure 14. Subplots a, b, and c are of the upper, fork, and span PIV measurement plane respectively. .... 56

Figure 21: Bar chart showing the CD of both morphologies at each PIV measurement plane, as well as those from previous studies listed in the order they appear in Table 2. .... 57

## List of Symbols and Acronyms

$A_R$ : Aspect ratio

AUV: Autonomous underwater vehicle

$C_D$ : Drag coefficient

$c$ : Mean chord length

$D$ : Sectional drag

$E_{11}$ : One dimensional fluctuating streamwise velocity spectra in the streamwise direction

$E_{12}$ : One dimensional fluctuating streamwise velocity spectra in the spanwise direction

$E_{13}$ : One dimensional fluctuating streamwise velocity spectra in the normal direction

$f$ : Caudal fin oscillation frequency

FOV: Field of view

FSI: Fluid structure interaction

$i$ : Interrogation window index

$\hat{K}_{xy}$ : Phase-averaged streamwise-spanwise turbulent kinetic energy

$\hat{K}_{xz}$ : Phase-averaged streamwise-normal turbulent kinetic energy

$k_1$ : Wavenumber in the streamwise direction

$k_2$ : Wavenumber in the spanwise direction

$k_3$ : Wavenumber in the normal direction

L: Characteristic length scale

l: Width of the wake region

PIV: Particle image velocimetry

Re: Reynolds number

r: Pixel-physical unit conversion factor

St: Strouhal number

TL: Total length

TKE: Turbulent kinetic energy

u: Velocity in the streamwise direction

$u_\infty$ : Free stream velocity

$\vec{u}$ : Velocity vector

$\hat{u}$ : Phase averaged streamwise velocity

$u'$ : Fluctuating streamwise velocity

$V_i$ : Velocity component in a given direction [i=1 is streamwise, i=2 is spanwise, i=3 is normal]

v: Velocity in the spanwise direction

$v'$ : Fluctuating spanwise velocity

W: Caudal fin span

$W_A$ : Wetted surface area of the model

w: Velocity in the normal direction

w': Fluctuating normal velocity

x: Streamwise direction

$x_i$ : Mean pixel displacement in corresponding direction [i=1 is streamwise, i=2 is spanwise, i=3 is normal]

y: Spanwise direction

z: Normal direction

$\nu$ : Kinematic viscosity of water

$\vec{\omega}$ : Vorticity vector

$\widehat{\omega}_z$ : Phase averaged normal vorticity

$\widehat{\omega}_y$ : Phase-averaged spanwise vorticity

$\Delta t$ : Time between images in a pair

$\rho$ : Density of water

$\hat{\tau}_{xy}$ : Phase-averaged streamwise-spanwise Reynolds shear stress

$\hat{\tau}_{xz}$ : Phase-averaged streamwise-normal Reynolds shear stress

$\epsilon_{31}$ : One dimensional fluctuating normal vorticity in the streamwise direction

$\epsilon_{32}$ : One dimensional fluctuating normal vorticity in the spanwise direction

$\epsilon_{21}$ : One dimensional fluctuating spanwise vorticity in the streamwise direction

$\varepsilon_{23}$ : One dimensional fluctuating spanwise vorticity in the normal direction

## 1.0 Introduction

Movement through an aquatic system can be affected by certain fluctuations in abiotic factors (temperature, currents, salinity, etc.) that have led sharks and other fishes to adapt in order to survive (locate prey, migrate, avoid predation, etc.). The field of *biomimicry* derives inspiration from the natural world for solutions that may be applied to technologies (autonomous underwater vehicles (AUVs), surface vessels, airplanes, etc.) to improve them and mitigate obstacles. For example, scientists may be inspired by the many different swimming modes (i.e. anguilliform or thunniform) utilized by fishes to move throughout their environments to design future biomimetic aquatic technologies (Suleman and Crawford, 2008). These different swimming methods are paramount to the successes of different pelagic organisms and can be influenced by certain morphological adaptations (e.g., fins, scales, mucous); for example, the important effect caudal fin morphology has on a fast, open ocean-dwelling shark species using the thunniform swimming mode for optimizing hydrodynamic efficiency during long migrations. While numerous studies have elucidated how different styles of locomotion and difference caudal fin morphologies affect locomotive efficiency in sharks (Wilga and Lauder, 2000; Copra, 1976; Sfakiotakis et al., 1999; Bernal et al., 2001; Graham et al., 1990), questions still remain open. One such question is the effect that caudal fin morphology has on the hydrodynamic performance when paired with thunniform oscillations. Shortfin Makos are a rarity among sharks in that they pair thunniform oscillations

with a lunate caudal fin. To examine possible differences in hydrodynamic characteristics between two different caudal fin morphologies when paired with thunniform undulations, this study took a multidisciplinary approach. Specifically, we constructed an oscillating scale model of a Shortfin Mako shark and measured the resulting hydrodynamic characteristics for two different caudal fins.

The caudal fin morphology was altered to examine how caudal fin morphology affected hydrodynamic performance. Reynolds number of a cruising Shortfin Mako (Du clos et al., 2018; Sepulveda et al., 2004; Motta et al., 2012) was used in constructing our model and experiments. The wake flow was measured using a non-intrusive flow imaging technique that allowed estimation of hydrodynamic forces acting on the shark. Results were compared with experimentally-obtained data from previous studies (Tamura and Takagi, 2009; Takagi et al., 2013) using tuna as a model species due to their ecological and physiological similarities to Shortfin Makos. Our results indicated that there is little difference in the hydrodynamic characteristics generated by the lunate caudal fin versus the heterocercal caudal fin at these Reynolds number and oscillation frequency. With the only difference shown by our results being the amount of rotational kinetic energy imparted to the wake, of which the lunate morphology generated slightly higher levels. These findings suggest that the lunate caudal fin has evolved to optimize motions not studied here such as acceleration, maneuvering, or lift.

This thesis is organized as follows, Section 2 presents background information relating to hydrodynamics, fish and shark locomotion, and the Shortfin Mako. Section 3 lays out the objectives of this research. Section 4 describes the experimental and data analysis methods. Section 5 presents results of the research. Conclusions and a summary of this study are presented in the final section.

## 2.0 Background

This study focused on the fluid-structure interaction (FSI) between an oscillating caudal fin of a Shortfin Mako shark paired with thunniform oscillations, and the surrounding fluid. Two different caudal fin morphologies were tested to characterize this phenomenon: lunate and heterocercal geometries, respectively. FSI involves the interaction of some solid or deformable structure and the surrounding or internal fluid and is characterized by static and dynamic interactions spanning multiple continuum fields. Such interactions may be exemplified by the interaction between a pipe and the fluid flowing within or a flexible wing and the flow moving over it.

The wake and possible vortex street (shown in Figure 1) behind an object immersed in a flow can sometimes be used to estimate the hydrodynamic forces acting on it. In equilibrium, steady-state and no acceleration, thrust equals drag. Measurement of the momentum deficit in the wake behind an object enables estimation of the momentum deficit, which may be used to estimate drag (Goett, 1939).

### 2.1 Fish Propulsion

The types of undulations performed by swimming fishes are not the same across all species. These undulations fall into four general modes: anguilliform, subcarangiform, carangiform, and thunniform (Breder, 1926; Lighthill, 1970; Webb, 1978; Lauder and Tytell, 2006;

Sfakiotakis et al., 1999), which are illustrated in Figure 2. Each of these modes corresponds to differing degrees of lateral extension over a defined body-length, with anguilliform and thunniform having the most and least respectively. By undulating, fishes generate a propulsive wake which meanders and may contain a vortex street which is a repeating pattern of positive and negative vortices. This wake may be further augmented by the fish if its median fins are angled with respect to the mean flow direction so that these fins have a vertical trailing edge. With this geometry, the fish imparts momentum into the flow more efficiently and reduces the size of the wake (Gray, 1953; Lighthill, 1970), which lessens the effect of pressure drag (Çengel and Cimbala, 2006).

The dominant source of drag experienced by a fish primarily depends on external factors such as flow conditions, proximity to the air-water interface, and differing relative conditions of gravitational, inertial, and viscous forces present in the flow (Fish, 1998). These sources of drag can be mitigated by utilizing morphological adaptations (e.g., median fins), innate behaviors (e.g., schooling), and secretion of materials (e.g., mucous). These biological factors are important to understand how fish species swim in various modes and at varying efficiencies.

Although body shapes of fish vary by species, the majority are streamlined. A streamlined body shape helps to delay flow separation as far back on the body as possible. Although not all fish species have a streamlined body shape, those considered to more closely resemble bluff bodies (those bodies with separated flow over a substantial part of its surface) still seek to mitigate drag and promote thrust. Flow separation occurs when the momentum at the surface of the body can no longer overcome the adverse pressure gradient which develops over the back-half of the surface under certain flow conditions (Bushnell and Moore, 1991; Anderson, 2010). Under these flow conditions, the separated flow will result in shear layers that merge from the trailing surface of the body and meander - and may mix downstream. This mixing forms an

unstable interaction, resulting in a series of vortices that may form an organized pattern under certain flow conditions (Çengel and Cimbala, 2006).

Morphological adaptations including caudal fin shape, body depth, along with kinematic differences between different swimming modes have major implications for hydromechanical efficiency, speed, and thrust generation. Relationships have been demonstrated to exist between parameters such as oscillation frequency and oscillation amplitude with thrust and efficiency (Xia et al., 2015). Direct relationships between forward velocity and oscillation frequency have been observed, and inverse relationships between oscillation amplitude and efficiency have been reported (Xia et al., 2015; Lighthill, 1970; Webb, 1984). The oscillation frequency of the caudal fin has been shown to have the greatest effect on hydromechanical performance (Akanyeti et al., 2017; Tytell, 2004) and is the largest contributing factor to increased thrust.

Most fishes combine lateral body undulations with oscillatory motions of their caudal fins to propel through the water (Sfakiotakis et al., 1999; Brooks and Green, 2019; Webb, 1984). Thrust and acceleration are generated to allow for forward propulsion, as well as the capture of prey, and evasion of predators. Certain fishes such as tunas and trout may also mitigate flow separation by controlling body-generated vortices and moving the separation point farther posterior on their bodies. Shifting the separation point posteriorly decreases the effect of pressure drag on the body (Çengel and Cimbala, 2006). A previously conducted study concluded that as fish undulate, their bodies generate vortices that are then passed posteriorly (Zhu et al., 2002). These body-generated vortices may be augmented by the fish to interact constructively or destructively with the vortices generated by the caudal fin. Pairing same sign body-generated vortices with caudally generated vortices results in constructive interference of the vortices at the wake and eventually leads to an increase in thrust. Whilst pairing opposite sign vortices from the body and caudal fin may result in destructive interference that increases propulsive efficiency but

decreases thrust generation (Zhu et al., 2002; Liang and Su, 2010). This negative interference was shown to be the case for tuna utilizing the thunniform mode of swimming, and for the giant danio utilizing the carangiform mode (Zhu et al., 2002). It has also been shown that certain fish with flexible median fins also may augment their swimming by utilizing the vortices shed from the trailing edge of these fins. At higher swimming speeds, the vortex street behind the dorsal fin of a bluegill sunfish combines constructively with the wake behind the body and this enhances its overall thrust generation (Drucker and Lauder, 2001; Tytell, 2006).

Different modes of undulation can also affect swimming efficiency (Chopra and Kambe 1977; Lighthill, 1960; Schouveiler et al., 2005). For those swimming organisms utilizing a mode with greater lateral oscillations, such as the carangiform or anguilliform modes, swimming efficiency decreases due to the effect of recoil on the body (Lighthill, 1969). The force that a swimming organism exerts on the surrounding fluid, is equal and opposite to the force that the surrounding fluid exerts back onto the swimming organism, assuming steady state (zero acceleration). Therefore, an organism that moves its body more while swimming, expends more energy to move and counteract recoil, thus, reducing efficiency. It has been demonstrated that those organisms performing carangiform oscillations generate higher thrust than thunniform swimmers, at the cost of hydromechanical efficiency (Li et al., 2012; Chopra, 1976). Hydromechanical efficiency of a flapping foil is the ratio of the work used for propulsion by the total amount of work expended through the flapping motion (Lighthill, 1970; Sfakiotakis et al., 1999).

For thunniform swimmers body oscillations are restricted to approximately the posterior one-third of the body with very little lateral head movement. This reduction in overall body movement helps to increase hydromechanic efficiency by decreasing the effect of recoil. High swimming efficiency does come at the cost of thrust generation, as thunniform swimmers must

beat their caudal fins faster and at greater amplitudes in order to accelerate (Xia et al., 2015). Body shape also has a significant effect on swimming efficiency. Thunniform swimmers have a fusiform body shape which includes a reduction in depth of the body's cross section, and a narrow caudal peduncle (Syme and Shadwick, 2011). The reduction in depth of the cross section is presumably to reduce the recoil experienced by the body as it oscillates. Because of this narrowing, the anterior section of the body has a significant drag reducing effect while not negatively affecting thrust generation (Lighthill, 1970).

## 2.2 Shark Propulsion

The 400 million year evolutionary history of sharks has seen them radiate and adapt to occupy nearly every oceanic habitat, from sedentary species on the sandy bottom, to those that constantly swim in the open ocean and never see the bottom (Sorenson et al., 2014). Most shark species have a tapered body with one or more dorsal fins, paired pectoral and anal fins (Thomson and Simanek, 1977). One of the main evolutionary differences distinguishing sharks from bony fish is their inability to directly control their buoyancy (Gleiss et al., 2017). As a group, sharks are muscle-bound and thus negatively buoyant, lacking the gas filled swim bladder that allows bony fish to hover in the water column. Sharks compensate in part for their negative buoyancy with an oil filled liver or fatty tissues (Cohen and Cleary, 2010). Despite this, sharks must generate their own lift (Moss, 1984; Flammang et al., 2011), meaning that most sharks swim constantly, which also allows water to move over their gills for respiration. Some sharks utilize ram ventilation (Graham et al., 1990), as they do not have branchial muscles strong enough to actively draw water over their gills and thus must mechanically force it by forward swimming. By utilizing ram ventilation, sharks can move at cruising speed without altering metabolic costs. Cruising speed is thought to be the minimum energetic cost for transport but this is unconfirmed (Lauder, 2015). The swimming efficiency of sharks is primarily dependent on parameters related

to their swimming mode (subcarangiform, carangiform, thunniform) and caudal fin morphology. Most sharks utilize carangiform swimming, while more specialized species adapted for high performance swimming also utilize thunniform. Using different morphological adaptations such as the caudal fin upper (epichordal) lobe, caudal fin lower (hypochoyrdal) lobe, median fin shape, or their dermal denticles may increase their hydrodynamic efficiency. Caudal fin geometry and its effect on hydrodynamic performance is discussed in greater detail in Section 2.4.

### 2.3 Lamnids and Scombrids

Thunniform swimmers, which includes scombrid fishes, cetaceans, and lamnid sharks, are thought to be the most efficient swimming organisms in the oceans (Liu et al., 2017) due to their need for constant forward motion and participation in long distance migrations. Because of this similarity, lamnids have convergently evolved to be ecologically and morphologically similar to scombrids (Syme and Shadwick, 2011; Shadwick, 2005). Shared morphological adaptations include internalized red muscle, narrow necking towards the caudal peduncle, endothermy, thunniform oscillations, and caudal fin geometry. Scombrid fishes are considered to be a prey item of certain lamnid sharks and this selective pressure may be another reason these distantly related families have convergently evolved. These fishes embark on long distance migrations, i.e., they must maximize their swimming efficiency - reaching the fastest cruising speed possible while expending a minimal amount of energy (Trump and Legget, 1980).

Many studies have been conducted to investigate the hydrodynamic characteristics of swimming fish (Triantafyllou et al., 1993; Wang et al., 2010; Wolfgang et al., 1999; Cohen and Cleary, 2010). In the specific case of thunniform swimming, the majority of studies on hydrodynamic characteristics have been relegated to studies involving tuna including numerical simulations, oscillating flat plates with lunate caudal fin geometries, scale physical models, and water tunnel tests with live individuals, due to the comparative ease of using tunas as a model

species rather than Lamnids like the Shortfin Mako (Yang et al., 2011; Hong and Chang-an, 2005; Wang et al., 2010; Takagi et al., 2013; Dewar and Graham, 1994). This choice primarily stems from the logistical difficulties involved with using Shortfin Makos as a model species, including capture, transport, husbandry, and cost. Simulations of tuna have, for example, quantified vorticity distributions in the wake, as well as observed the interactions of constructive and destructive interference between bodily-shed vortices and caudal fin-shed vortices (Gopalkrishnan et al., 1994; Zhu et al., 2002). Simulations of a tuna wake by Xia et al., (2015) determined that the resulting wake consists of a series of disconnected sickle-shaped vortices consistent with observations in nature (Anderson, 1996) (see Figure 3). Xia et al., (2015) also suggested that thunniform swimmers achieve high cruising speeds with high hydromechanical efficiency. Such studies have provided information regarding the expected hydrodynamic characteristics generated by organisms employing the thunniform swimming method. While these characteristics have yet to be confirmed using a lamnid shark as the model species instead of tunas, the ecological and morphological similarities between the two distantly related species suggest that lamnids would generate similar characteristics.

#### 2.4 Caudal Fin Morphology

Caudal fin geometry plays a role in aquatic organisms locomoting efficiently through their environment. It is hypothesized that the wide variety of caudal fin geometries observed in nature each serve a different hydrodynamic purpose for those species, particularly those that rely on the caudal fin for primary thrust generation. An important characteristic of the caudal fin geometry is the aspect ratio ( $A_R$ ), defined as:

$$A_R = \frac{W}{c} \quad [1]$$

where  $W$  is the span of the caudal fin and the mean chord length is  $c$ . Previous studies have found that varying the  $A_R$  will significantly change propulsive performance and wake patterns (Dong et al., 2006; Raspa et al., 2014; Yeh and Alexeev, 2016)

Slower moving species that prioritize burst acceleration and maneuverability usually have lower aspect ratio caudal fins. It has been shown that lower aspect ratio caudal fins generate greater thrust when accelerating or maneuvering, which is important for evading predators or capturing prey (Liu and Dong, 2016; Cheng and Murillo, 1984; Flammang and Lauder, 2009) but generally operate at a lower hydromechanical efficiency (Lee et al., 2017). Faster moving species that prioritize sustained swimming and efficiency generally have high aspect ratio caudal fins (Lighthill, 1969; Chopra, 1974; Sagong et al., 2013, Liu and Dong, 2016). High aspect ratio caudal fins are normally seen on those species that also employ the thunniform mode of swimming. This pairing, while efficient, has been shown to generate slightly less thrust than lower aspect ratio caudal fins (Lee et al., 2017).

A shark's caudal fin serves important functions such as propulsion and generating enough lift to counteract a shark's naturally negatively buoyant body (Lighthill, 1975). The fastest moving and the most hydromechanically efficient sharks all belong to the family Lamnidae, which have high aspect ratio lunate caudal fins (Shadwick, 2005). Lunate caudal fins have been described as a two-dimensional airfoil (Lighthill, 1969), with a rounded leading edge and a sharp trailing edge. This morphology is characterized by the epichordal (upper) and hypochordal (lower) lobes being of approximately the same shape and size with a rounded leading edge and a sharp trailing edge, similar to that of scombrid fishes. As previously mentioned, high aspect ratio caudal fins have been shown to generate slightly lower levels of thrust compared to caudal fins with lower aspect ratios and this reduced thrust is speculated to be due to the pairing of thunniform oscillations with the lunate caudal fin. This pairing elicits an increase in risk of leading-edge separation

(Chopra, 1976) because of the amount of leading-edge suction acting on the fin. Leading-edge separation greatly reduces thrust and efficiency. To generate high thrust, Chopra (1976) argues that lunate tailed organisms need to swim at a high angle of attack, which is the angle between the plane of the lunate caudal fin and the incoming flow. During steady forward locomotion, the oscillating caudal fin generates a forward thrust force, which acts on the center of mass of the shark (Thomson and Simanek, 1977). Through each lateral oscillation, force is simultaneously directed horizontally and upwards, counteracting drag and gravity. Regardless of caudal fin morphology or swimming mode, the thrust force consists of two components: i) the along-body force that is associated with the thrust directed horizontally during each lateral caudal beat and is dependent on the angle of the caudal fin with respect to the oncoming flow (Thomson and Simanek, 1977) and ii) the transverse force that is the thrust directed upwards (normal to the body) as a result of the caudal fin rotating about the vertical spanwise plane.

A majority of shark species pair carangiform oscillations with a lower aspect ratio heterocercal caudal fin. Heterocercal caudal fins are characterized by having a larger epichordal lobe, and smaller hypochordal lobe. This pairing of oscillations and caudal fin morphology have been shown to generate greater thrust with less hydromechanic efficiency than thunniform swimmers utilizing a lunate caudal fin (Lee et al., 2017). The lower aspect ratio heterocercal caudal fin has a higher burst potential (e.g., for predator evasion or prey capture) but still allows for long distance migration (Turner et al., 2020; Reyier et al., 2008). One difference between the lunate and heterocercal caudal fin morphologies, other than the aspect ratio, is its flexibility. Both lobes of the lunate caudal fin are known to be rigid, while the heterocercal caudal fin lobes are more flexible (Crofts et al., 2019). This dissimilarity in flexibility may attribute to the differences in hydromechanical efficiency between the two morphologies due to the increased recoil experienced by the heterocercal morphology. Certain species, which pair carangiform oscillations

with a heterocercal caudal fin morphology, have been investigated using techniques similar to that used in this study. Wilga and Lauder (2002) investigated the caudal fin hydromechanics of Leopard sharks and found that their oscillating caudal fin produces a dual vortex ring, which is an enclosed loop of fluid in the wake of the caudal fin and is shown in Figure 4. The first vortex ring forms at the end of every tail beat, with the second ring attaching inside the first as it is generated by the following tail beat. This finding, however, is not well supported by the data in the study. The orientation of the dual vortex ring was assumed by Wilga and Lauder (2002) as evidence that the function of a heterocercal caudal fin provides torque around the shark's center of mass. Simulations involving an oscillating heterocercal caudal fin, however, have shown that the vortices shed from the upper lobe are stronger than those from the lower lobe because of the larger amplitude of the oscillations of the upper lobe (Liu and Dong, 2016).

The highly specialized lunate caudal fin morphology has (in combination with other characteristics) allowed high-performance pelagic predators to achieve success. This morphology has convergently evolved in the majority of swimming organisms that use the thunniform swimming mode. The shape of the caudal fin is not the only important factor the kinematics of the fin are also important (Wilga and Lauder, 2000). An oscillating caudal fin may change orientation such that the trailing edge shape varies throughout a tail beat cycle. Certain species, such as the bluegill sunfish, possess a flexible caudal fin made of individual fin rays connected by tissue that can be directly controlled to change the trailing edge shape and thus augment certain hydrodynamic characteristics, such as vorticity. While other species, such as the Bluefin tuna, have a rigid caudal fin with a rounded leading edge and sharp trailing edge that cannot be directly controlled. A rigid caudal fin with a rounded leading edge allows the fish to take advantage of water moving sharply around it, generating a leading-edge suction force parallel to the chord of the fin (Sane, 2003), while having a sharp trailing edge promotes organized vortex shedding

(Lighthill, 1969). An organized vortex sheet transfers momentum more efficiently than one that is unorganized and may lead to a narrower wake therefore reducing the drag force acting on the fin (Han et al., 2017; Xia et al., 2015). For example, experiments have shown that tunas generate more concentrated vorticity in their wake than other species (i.e., trout). This concentrated vorticity may be a reason that tunas have been found to be more hydromechanically efficient than those with a lower aspect ratio caudal fin such as trout. Hydromechanical efficiency for these two species have been calculated as  $\sim 0.164$  for the trout and  $\sim 0.252$  for the tuna, an increase of 54% (Liu and Dong, 2016).

## 2.5 Shortfin Mako Shark

The Shortfin Mako (*Isurus oxyrinchus*) is a large, pelagic, fast swimming, migratory, and purportedly the fastest shark species found in all temperate and tropical seas. They are capable of bursts up to  $19 \text{ ms}^{-1}$  (Afroz et al., 2016; Compagno, 2001), but are normally found cruising at approximately  $0.64 \text{ ms}^{-1}$  to conserve energy (Sepulveda et al., 2004) with a tail oscillation frequency of 1 Hz (Sepulveda et al., 2007). Shortfin Makos are an exclusively pelagic species that never stop swimming for their entire lives. Shortfin Makos also feed on fast-moving teleost fish such as tuna, bluefish, and billfish. Shortfin Mako's are more ecologically and morphologically similar to scombrids than other members of the lamnid family (Syme and Shadwick, 2011). Due to their need for constant forward motion, long distance migrations, and their similarities to scombrids, Shortfin Makos are thought to be extremely hydromechanically efficient.

Shortfin Makos have several physiological evolutionary adaptations that are utilized to achieve these high speeds and efficiency of movement. The adaptations that contribute to this include ridged dermal denticles, internalized red muscle, large gill slits, a torpedo shaped body, lunate caudal fin (Figure 5), and thunniform swimming mode (Du Clos et al., 2018; Sepulveda et al., 2004; Carey and Teal, 1969). The increased cruising speed is further facilitated by Shortfin

Makos being endothermic while most other shark species are ectothermic (Harding et al., 2020). These adaptations allow Shortfin Makos to have a lower caudal beat frequency compared to other shark species but still swim at comparable cruising speeds (Graham et al., 1990); and this unique pairing of a lunate caudal fin with thunniform oscillations could be related to the Shortfin Makos' rapid swimming (Stevens, 2008). Shortfin Makos do however increase their caudal oscillation frequency and lateral head movement when accelerating, an action typical of predation and predator avoidance. This increased lateral motion may affect their hydrodynamic performance and is not considered in this study, which focuses on steady swimming. Other previous studies using shark species with heterocercal caudal fins have provided insight on associated hydrodynamic characteristics (Turner et al., 2020; Wilga and Lauder, 2002; Fish and Lauder, 2006). The hydrodynamic characteristics of the Shortfin Mako have not yet been studied primarily due to the logistical challenges previously discussed. Using a model of the Shortfin Mako for our experiment allows us to bypass those logistical challenges and increases the knowledge base of this species, as well as investigates the role of caudal fin morphology when paired with thunniform oscillations. Thus, our study sought to investigate certain hydrodynamic characteristics of the Shortfin Mako by utilizing an oscillating scale model with two different interchangeable caudal fin morphologies to determine the effect caudal fin morphology has on these certain hydrodynamic characteristics when paired with its natural thunniform swimming mode.

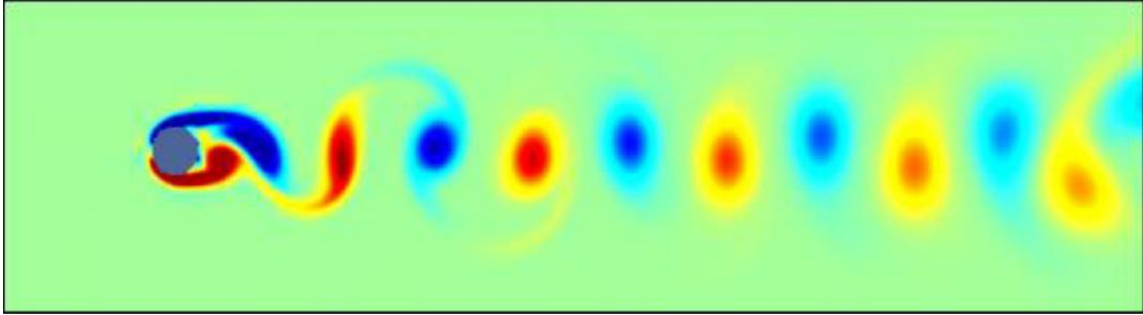


*Figure 1: Vortex street behind a cylinder with flow moving from left to right, red indicating positive vorticity, and blue indicating negative vorticity (image provided courtesy of Krishnamoorthy Krishnan).*

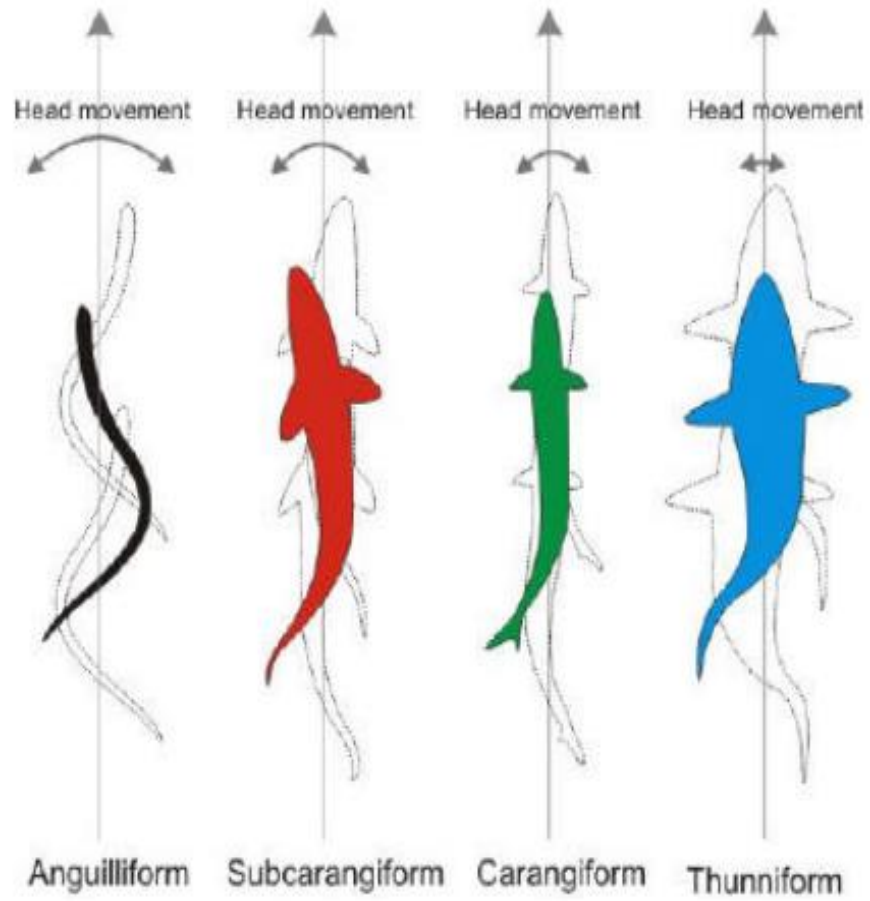


Figure 2: Depiction of the 4 most common fish swimming modes, with thunniform swimming being the focus of this study. *Fish Physiology*, (1978).

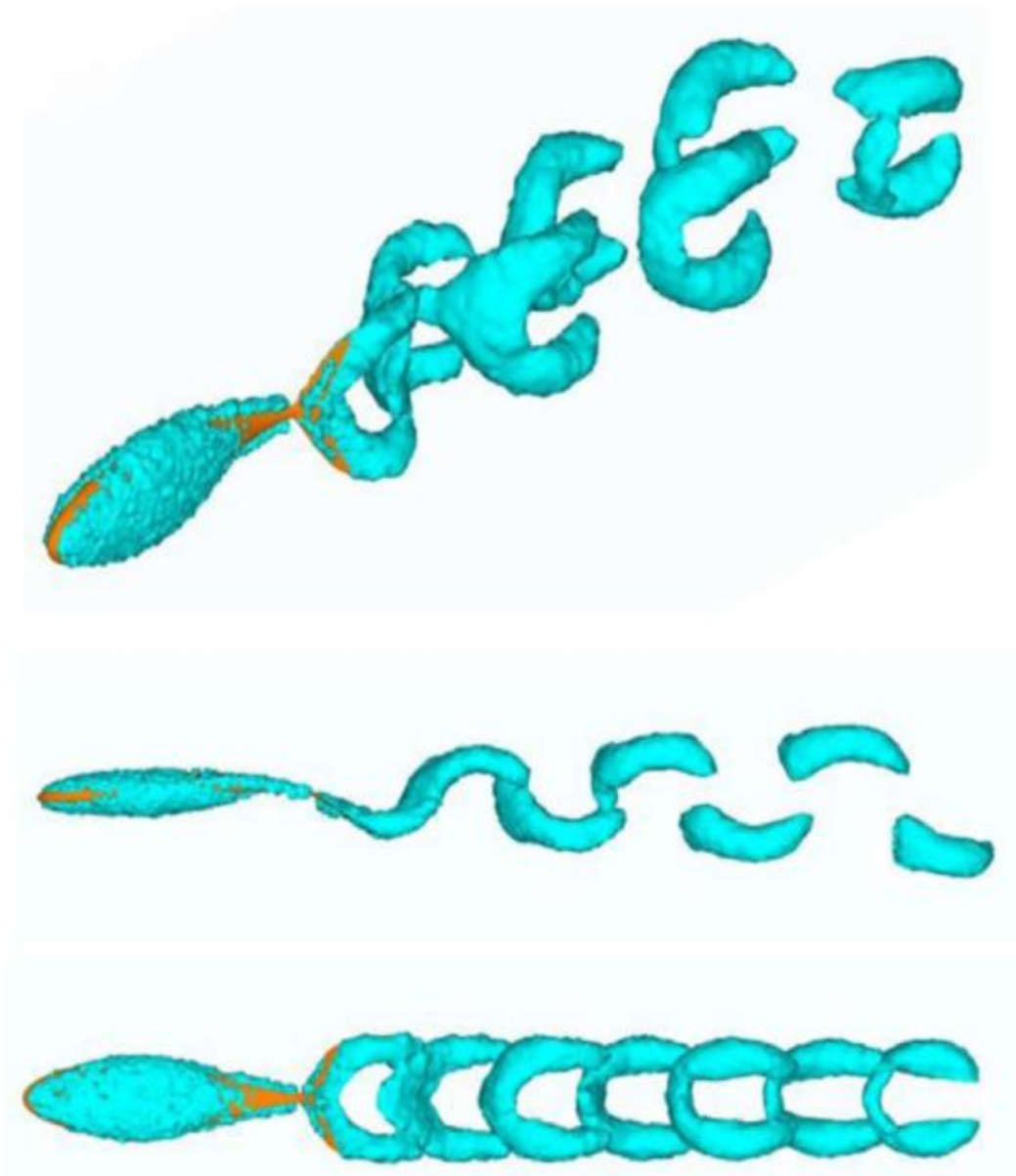


Figure 3: Three-dimensional wake structure of a tuna showing the sickle-shaped vortices. From Xia et al., (2015).

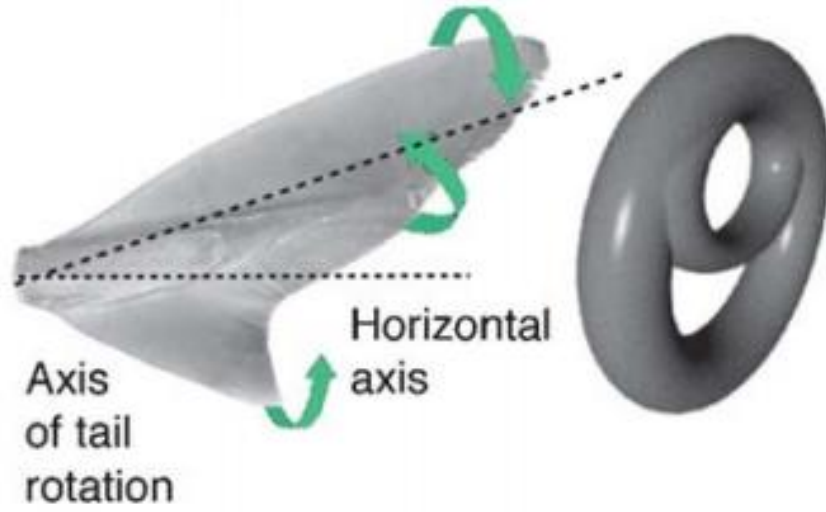


Figure 4: Dual ring vortex structure in the wake of a heterocercal caudal fin. From Fish and Lauder, (2006).

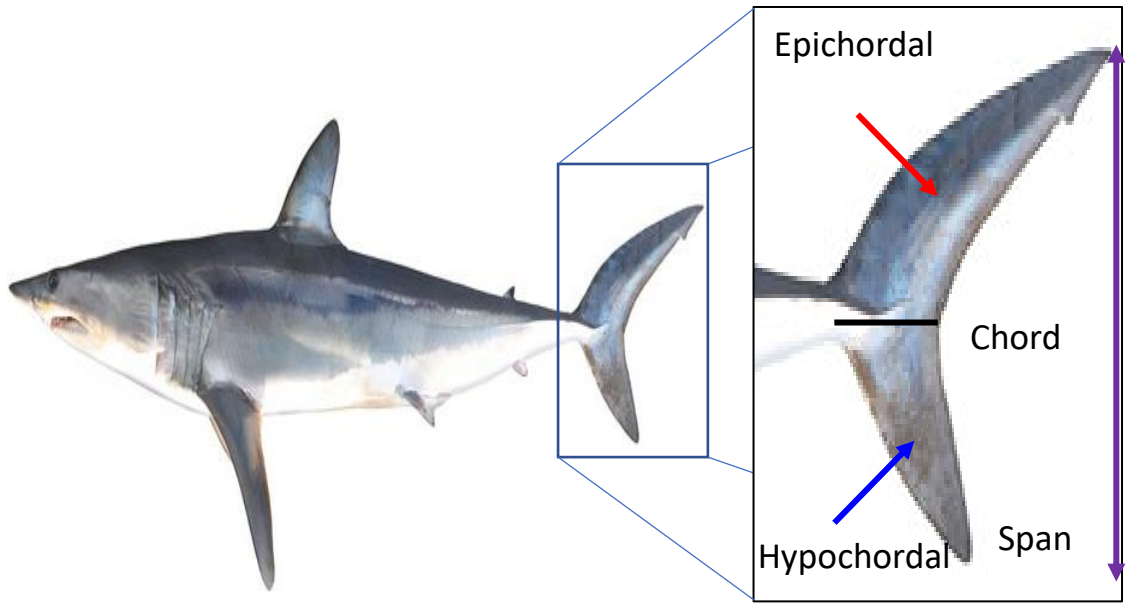


Figure 5: Image of a shortfin Mako shark with its caudal fin enlarged to show the hypochordal lobe, epichordal lobe, chord, and span. Source: CSIRO National Fish Collection. License: CC-BY-Attribution.

### 3.0 Research Objectives

In order to better understand the effect of caudal fin morphology on the hydrodynamics of the Shortfin Mako shark (*Isurus oxyrinchus*) during steady thunniform swimming we investigated a high aspect ratio lunate caudal fin and lower aspect ratio heterocercal caudal fin at a predetermined caudal oscillation frequency. To accomplish this, we i) examined and compared the wake characteristics behind an oscillating Shortfin Mako model with two distinct caudal fin morphologies, and ii) investigated the effect caudal fin morphology has on the drag of Shortfin Makos when paired with thunniform oscillations. The model used was 50 cm in length made of a silicone mixture with geometry based on a 3D rendering of a Shortfin Mako. Our research was an experimental investigation conducted utilizing particle image velocimetry (PIV) in a flume to measure flow components in two planes at three locations in the near wake of both caudal fin morphologies. The streamwise velocity,  $u$ , and spanwise velocity,  $v$ , components were measured in the streamwise-spanwise ( $x, y$ ) plane, and measurements of the  $u$  and vertical velocity,  $w$ , were measured in the streamwise-normal ( $x, z$ ) plane using the same technique, which will be referred to as the PIV “span” measurements in the remainder of this document. Hydrodynamic forces were estimated from the momentum deficits present in the wake behind the model (Goett, 1939), and turbulence characteristics were calculated from the velocity components. Results were phase averaged into left and right phases to account for the unsteady motion of the model and the flow. These quantities and comparisons between morphologies provided insight into the effect caudal fin morphology has on the hydrodynamic performance of the Shortfin Mako.

## 4.0 Methods

Measurements of the hydrodynamic forces and wake flow characteristics of an oscillating Shortfin Mako shark model with two distinct caudal fin morphologies were performed in the flume located at the *Environmental Fluids Laboratory* (EFL) at Coastal Carolina University. Near wake flow measurements at two streamwise-spanwise and one streamwise-normal PIV measurement planes behind each morphology were taken. The experimental setup and methods used to analyze the data are explained below.

The oscillating scale model of a Shortfin Mako is described in subsection 4.1, subsection 4.2 and 4.3 describe the experimental facility and flow measurement techniques respectively, subsection 4.4 details the experiments, and this section concludes with subsection 4.5 covering the data analysis methods applied to the flow measurements for addressing the research objective described in section 3.

### 4.1 Shortfin Mako Model

The model used in this study was based on a 3D drawing (TurboSquid.com), shown in Figure 6, and was rendered for our purposes in the 3D modeling software SolidWorks. The model total length (TL) was 50 cm, which equates to a 6:1 scale model of a 3 m adult Shortfin Mako. A negative of this Shortfin Mako model was used to generate a mold.

The exterior shell was 3D printed using Onyx plastic filament (Markforged Onyx One). A mix of carbon and nylon served as the printing material for the mold, with pieces printed

individually and then combined to form the entire mold (Kulkarni et al., 2017), as shown in Figure 7. The mold for the alternate heterocercal morphology was printed separately and attached to the existing model once the original lunate morphology was removed, this alternate morphology was derived from an image of a Blacktip Shark (*Carcharhinus limbatus*) and is shown in Figure 8. Recall, we chose to add the heterocercal caudal fin for comparison because it is the common morphology to most other shark species. To add flexibility to the model, Dragon Skin platinum cure silicone mixed with paint thinner was cast into the mold and allowed to cure. Paint thinner was added to the silicone mixture to generate a material that closely mimicked the flexibility of a living shark. No sample of a Shortfin Mako was readily available so a sample from a deceased Lemon Shark was used to determine flexibility, assuming that bodily flexibility of shark skin is generally consistent across species. The Young's modulus of the Lemon shark sample was found to be  $1.0 \times 10^3$  Pa which is similar to what has been used in previous studies (Epps et al., 2009; Turner et al., 2020). A mixture of 80% silicone and 20% paint thinner generated a material with a Young's modulus of  $1.1 \times 10^3$  Pa. Caudal fin flexibility is not consistent across morphologies in nature (see Section 2.2) with the lunate morphology known to be more rigid than the heterocercal morphology; however, we could not account for this difference in the current study due to a lack of data on the differing material properties of the two caudal fins. Thus, both caudal fin morphologies has approximately the same flexibility.

Lateral caudal oscillations closely resembling the thunniform swimming mode were generated by a small servo motor embedded inside a protective housing within the mold before the silicone was poured. The servo was controlled via an Arduino microcontroller and powered by 6V batteries. The caudal beat frequency was set to 0.4 Hz to obtain a Strouhal number within an optimal range (Triantafyllou et al., 1993) which for fish is between 0.25 and 0.45. The actuation of this servo degraded over time presumably due to saturation of the model in the water despite

our best efforts to waterproof the servo housing; this degradation of the actuation, which became more step-like over time, could be a source of error in the experimental results.

A support plate was also placed within the model attached to the back (tailward side) of the protective housing around the motor. This plate served as an anchoring point for the model, as well as for directing the torque produced by the motor posteriorly. The rotor arms of the servo motor imparted torque on a vertical swim plate located in the posterior end of the model, causing the caudal to oscillate laterally. This lateral motion was facilitated by attaching two C-shaped inserts to the inside of the mold before pouring the silicone. These inserts created a natural pivot point for the model, mimicking that of thunniform swimmers. Inside the caudal fin a plastic insert provided extra support to regions of the fin that were relatively thin. Each of these components may be seen in Figure 9. Each caudal fin morphology was spray painted black to minimize any laser reflections during the flow measurements.

The model was positioned in the center of the flume to avoid any interference from the walls and surface of the flume. This positioning was accomplished by inserting a threaded anchoring rod into the support plate on one end and into a cross-bar secured across the span of the flume on the other end. Any turbulence produced by these mounting structures was assumed to be small enough not to interfere with the wake produced by the model (Adaramola et al., 2006).

#### 4.2 Facility

Experiments took place in a recirculating open channel flow facility (flume) with an overall length of 15 m and a cross section of 0.7 m × 0.5 m. A centrifugal pump controlled by a variable frequency drive generated flow rates up to 3 m<sup>3</sup>/min, transferring water between two large, circular reservoirs at each end of the channel; each reservoir could hold over 6.5 m<sup>3</sup> of water. A 5

m long glass section in the middle of the trough allowed for visualization of the flow. At the exit of the upstream reservoir a funnel and set of screens served to straighten the flow as it entered the trough, while flow restrictors (a series of vertical, cylindrical pipes) at the exit of the trough served to maintain a constant water level across the trough and prevented wave reflections from the downstream reservoir reverberating back into the flume. An isometric drawing of the flume is shown in Figure 10. Water temperature was maintained by the surrounding ambient room temperature and was normally 20-22 °C.

#### 4.3 Particle Image Velocimetry

Flow measurements were obtained using particle image velocimetry (PIV). PIV is a nonintrusive optical flow measurement technique measuring 2D/3D velocity fields in a plane/volume (Raffel et al., 1998; Taylor et al., 2010; Adrian and Westerweel, 2011). The development of PIV targeted investigation of turbulent flows. PIV is based on using seeding particles, a light source (e.g., a laser), and an imaging device (e.g., a digital camera) to capture a series of images, which in turn yield velocity vector maps. The seeding particles allow for indirect measurement of the velocity by serving as tracers, acting as a proxy for the flow. A pair of consecutive images are captured for the estimation of average particle displacement between the images in this pair; a time series of these image pairs are collected (Adrian, 1991; Raffel et al., 1998). For this experiment, microscopic (mean 11  $\mu\text{m}$  diameter), neutrally buoyant, and chemically inert glass sphere beads were used as seeding particles. These particles were in good agreement with recommended tracer particle characteristics from the literature (Adrian, 1986; Melling, 1997). A dual pulsed laser, a series of optical lenses, and a mirror were used to create a thin light sheet (approx. 1 mm thick) that illuminated the flow and tracer particles. The laser was a high-powered Neodymium doped: yttrium-aluminum-garnet (Nd-YAG) laser, emitting a monochromatic green light with power up to 140 mJ/pulse at a wavelength of 532 nm. The two

laser heads were contained in a protective housing and synchronized to emit double pulses at set time intervals. To generate a light sheet of appropriate thickness, the laser passed through a series of optics. Beginning with a concave cylindrical lens that changed the laser from a beam to a sheet, then through a spherical lens that narrowed the sheet to the desired thickness which was approximately 1 mm. Particle distributions were captured by a camera imaging perpendicular to the light sheet. We used a synchronizer to set the timing between laser pulses and the camera. A CCD double exposure camera with 29-million-pixel resolution, double exposure frame rate maximum of 2 Hz, and a dynamic bit depth of 12 was used to capture images of the illuminated particles. A Nikon AF DC-Nikkor 105 mm lens was attached to the front of the camera combined with a Kenko 12 mm extension tube for increased magnification which yields a more dynamic velocity range (Adrian, 1997).

The laser illuminated the streamwise spanwise ( $x, y$ ) plane which was used to measure velocities at two locations for each morphology, at the upper lobe and fork. Illumination of the streamwise-spanwise plane can be seen in Figure 11. Measurements at the upper lobe were taken 1 cm down from the tip of the lobe of each morphology. By illuminating the streamwise-spanwise plane we were able to measure the  $u$  and  $v$  components of velocity. To illuminate the PIV span plane ( $x, z$ ), the laser was placed below the flume and the beam directed horizontally at a  $45^\circ$  mirror so that it reflected upwards at a  $90^\circ$  angle, then through the series of optics, and thus illuminated the span plane ( $x, z$ ) directly posterior to the caudal fin. The optical setup for measuring both PIV planes was the same. Using this setup, we measured the  $u$  and  $w$  components of velocity. We collected 1200 image pairs in each experiment to ensure statistical convergence.

#### 4.3.1 PIV Image Analysis

The average displacement of tracer particles was computed using correlation analysis. This analysis was performed in  $64 \times 64$  pixel<sup>2</sup> interrogation windows for all image pairs (consecutive

images). Estimated velocity was calculated by dividing the average displacement in each interrogation window by the time between images. Particle displacement in pixels was converted to a velocity using an image of a calibration target with markers in a grid at known intervals and the time between images in a pair. This conversion of particle displacements into physical units is:

$$V_i = \frac{x_i}{\Delta t} r \quad [2]$$

with  $V_i$  representing a velocity component in either direction ( $u$ ,  $v$ , or  $w$ ),  $\Delta t$  is the time between images in an image pair,  $x_i$  is the mean pixel displacement in the corresponding streamwise, spanwise, or normal direction ( $x$ ,  $y$ , or  $z$ ) within each interrogation window,  $r$  is the pixel-physical unit conversion factor taken from the calibration target and the subscript  $i$  denotes the interrogation window index.

Data were cross correlated for each interrogation window with 50% overlap between adjacent windows (Willert and Gharib, 1991). A signal to noise ratio threshold of 1.5 was implemented to avoid any bias from spurious vectors (Gui et al., 2002), where the highest cross-correlation peak was the signal, and the second highest cross-correlation peak was considered as the noise. The process is shown in Figure 12.

Some vectors that passed the signal to noise threshold may still be spurious, on the order of 1-3% (Raffel et al., 1992) of all the vectors, therefore two additional filters were applied during post-processing. These two additional filters were a global filter and a local filter. First, the global filter was applied to every vector map and removed any vectors more than 3 standard deviations from the map mean pixel displacement. The second localized filter removed erroneous displacement vectors greater than  $\pm 2$ -pixel displacements from the surrounding  $5 \times 5$  vector neighborhood median (Nogueira et al., 1997). Filtered vectors were interpolated using the median

value from vectors in the surrounding 5×5 neighborhood to fill vacancies with approximated vectors. This process was performed iteratively starting with regions with the least missing vectors until all gaps had been filled.

#### 4.4 Experiments

Two different caudal fin morphologies were examined in conjunction with thunniform oscillations using PIV to measure flow velocities at three locations. Water height in the flume was 38 cm to ensure the model was fully submerged. Approximate streamwise flow velocity was set to 0.20 m/s, to most closely match the Reynolds number of a swimming Shortfin Mako with that of the model (see next subsection). The matrix of experiments is presented in Table 1, including associated parameters.

##### 4.4.1 Reynolds Number

The non-dimensional Reynolds number ( $Re$ ) represents the ratio between inertial to viscous forces and is sometimes used as a threshold for the onset of turbulence:

$$Re = \frac{u_{\infty}L}{\nu} \quad [3]$$

with  $u_{\infty}$  as the free stream velocity,  $L$  as the characteristic length scale, which for this study was the total length of the model, and  $\nu$  is the kinematic viscosity of water. Freestream velocity was estimated from the PIV data as the (spatial and ensemble) mean streamwise velocity taken from areas showing nearly uniform flow in the streamwise direction (i.e., outside the wake). An adult, 3 m TL Shortfin Mako swims at a Reynolds number of  $3.0 \times 10^6$ . To most closely replicate the flow conditions of a cruising Shortfin Mako, the Reynolds number for the lunate and heterocercal morphologies were  $1.0 \times 10^5$ , and  $1.12 \times 10^5$  respectively. These Reynolds numbers are an order of magnitude lower than that observed in the natural environment but was the largest Reynolds number possible for this facility.

#### 4.4.2 Strouhal Number

The  $St$  is a nondimensional number, which may be used to characterize propulsive efficiency in swimming organisms. Efficient propulsion of aquatic organisms falls within a narrow range of Strouhal numbers, between 0.25 and 0.45 (Triantafyllou et al., 1993), and is defined as:

$$St = \frac{fl}{u_{\infty}} \quad [4]$$

where  $f$  is the caudal fin oscillation frequency, and  $l$  is the width of the wake. In this study, we take  $l$  to be equal to the maximum excursion of the caudal fin's trailing edge as it oscillates. Shortfin Makos normally cruise at an estimated Strouhal number of 0.36 given their caudal fin oscillation frequency, and cruising velocity (Sepulveda et al., 2007; Donley et al., 2005; Klimley et al., 2002). For this experiment, the  $St$  of the model was 0.26, which falls within the range of efficient propulsion, and is similar to observations of Shortfin Makos in nature (Sepulveda et al., 2007; Donley et al., 2005; Klimley et al., 2002).

#### 4.5 Data Analysis

Collected PIV data was analyzed to estimate hydrodynamic forces and characterize turbulence-caudal interactions. PIV measurements of the two components of the near wake flow velocities were performed. Vorticity, drag coefficients, Reynolds stresses, turbulent kinetic energies, and velocity and fluctuating vorticity spectra were estimated. The results were compared with previous experiments (e.g., bluefin tuna) to look for similarities across similar species.

Because the caudal fin was oscillating, both the caudal and the flow past it were considered to be in unsteady motion. As a result of this unsteady motion, the ensemble mean could not be used to characterize the wake. Considering the caudal fin oscillated at 0.4 Hz and the PIV camera had a frame rate of 1 Hz for this experiment, we were able to capture a maximum of

2 images per tail beat period. Thus, estimation and comparison of wake characteristics of each morphology was achieved by separating the images into phases; the leftmost and rightmost excursions of the caudal fin for images taken in the streamwise-spanwise plane, and the mid phase for images taken in the span plane. These phases are depicted in Figure 13. Organization of individual images was done visually for all experiments, where any images not considered to be sufficiently at the leftmost, rightmost, or mid position were removed from the data analysis. Flow quantities were subsequently phase averaged over the set of PIV frames corresponding to each “left”, “right”, and “mid” phase, and denoted with a caret (^) above the variable. These results give insight into the hydrodynamic characteristics and thrust generation of each caudal fin morphology when paired with thunniform oscillations.

#### 4.5.1 Vorticity

As the caudal fin oscillates, in certain instances one may conceptually view one vortex forming at the upper side of the fin, and one on the lower side that are shed into the wake when the fin reaches its most lateral position and changes direction (Muller et al, 1997). The tendency of the fluid to rotate is defined as the vorticity ( $\vec{\omega} = \nabla \times \vec{u}$ ). Thus, the phase-averaged vorticity should result in an upper region of positive vorticity, and a lower region of negative vorticity. Such a pattern could indicate the presence of a reverse von-Karman vortex street (Bao and Tao, 2014; Muller et al., 1997; Williamson and Roshko, 1988). Phase-averaged normal vorticity,  $\widehat{\omega}_z(x, y)$  was estimated from PIV measurements in the streamwise-spanwise plane at both locations (i.e., upper lobe and fork) for both morphologies. Phase-averaged spanwise vorticity  $\widehat{\omega}_y(x, z)$  was estimated from PIV span measurements at the mid phase for both morphologies.

#### 4.5.2 Reynolds Shear Stresses

Transfer of momentum in turbulent flows occurs through eddying motions (Reynolds, 1895). This transfer of momentum in a fluctuating velocity field gives rise to the Reynolds stresses

(Pope, 2001). Phase-averaged Reynolds shear stress per unit density ( $\hat{\tau}_{xy}$ ) for the streamwise-spanwise PIV plane is defined:

$$\hat{\tau}_{xy} = -\widehat{u'v'} \quad [5]$$

where  $u'$  and  $v'$  are the fluctuating streamwise and spanwise velocity components, and for the streamwise-normal plane:

$$\hat{\tau}_{xz} = -\widehat{u'w'} \quad [6]$$

where  $w'$  is the fluctuating normal velocity component. These Reynolds shear stresses are computed at all locations in the PIV measurement planes.

#### 4.5.3 Turbulent Kinetic Energy

Turbulent kinetic energy (TKE) is a measure of the average kinetic energy per unit density that is a result of friction-induced fluid shear within a fluctuating velocity field. This energy ultimately dissipates as a result of viscous forces after it is transferred down the turbulence energy cascade (Pope, 2001). TKE is defined (Pope, 2001) as half the trace of the Reynolds stress tensor, which is the sum of two normal turbulent stresses in the 2D measurement plane. Thus, for the streamwise-spanwise planes:

$$\hat{K}_{xy} = \frac{1}{2}(\widehat{u'^2} + \widehat{v'^2}) \quad [7]$$

and for the streamwise-normal plane:

$$\hat{K}_{xz} = \frac{1}{2}(\widehat{u'^2} + \widehat{w'^2}) \quad [8]$$

Phase-averaged TKE was estimated for both caudal fin morphologies at all locations for all PIV measurement planes.

#### 4.5.4 Spectra

The kinetic energy is generated by the oscillating caudal fin and imparted to the flow at large scales, and is transferred to smaller scales through eddying motions, where it ultimately dissipates at the smallest scales to heat. Between these two scales, at high Reynolds numbers, exists the inertial subrange where energy is transferred from larger to smaller eddies assuming negligible dissipation (Josserand et al., 2017). To show how translational and rotational kinetic energy were distributed with scale in the wake, energy spectra were calculated for fluctuating velocity and vorticity. The resulting fluctuating velocity and vorticity spectra are described in the results section (Section 5.1.1) and represented as  $E_{11}$ ,  $E_{12}$ , and  $E_{13}$ , with the first subscript representing the fluctuating velocity component, and the second subscript representing the direction (1=streamwise, 2 =spanwise, 3 = normal). For example,  $E_{11}$  represents the spectra of fluctuating streamwise velocity when calculated in the streamwise direction. Similarly, the resulting fluctuating vorticity spectra are represented by  $\epsilon_{31}$ ,  $\epsilon_{32}$ ,  $\epsilon_{21}$ , and  $\epsilon_{23}$ . In this case, the first subscript represents the fluctuating vorticity component, and the second subscript represents the direction. For example,  $\epsilon_{31}$  represents the fluctuating normal vorticity in the streamwise direction.

These calculations involved several steps. First, streamwise distributions of the fluctuating streamwise velocity (or fluctuating normal vorticity) of each phase are detrended to remove any linear trends along this direction. A hamming window was applied (Mockett et al., 2010; Scarano, 2001) to the data and power spectral density (PSD) was calculated from a 32-point fast Fourier transform. Results were subsequently ensemble averaged across all (streamwise) rows of each PIV map, and for all frames of each phase. This procedure was also applied for computing spectra of fluctuating streamwise velocity and normal fluctuating vorticity along the spanwise direction for each applicable PIV dataset for both morphologies. Similarly, streamwise

and normal distributions of fluctuating streamwise velocity and fluctuating spanwise vorticity were used to compute corresponding spectra for both morphologies.

#### 4.5.5 Hydrodynamic Forces

A Shortfin Mako cruising at a steady forward velocity has four primary forces acting on it; lift, buoyancy, drag, and thrust. While cruising, in accordance with Newton's 3<sup>rd</sup> law, thrust and drag are equal. To calculate the drag force and drag coefficient, we used the phase-averaged streamwise velocity spanwise and normal profiles measured by PIV. Drag was estimated using the momentum equation based on Goett (1939), who demonstrated sectional drag to be directly related to the velocity deficit in the wake:

$$D = \rho \int_0^l \hat{u}(u_\infty - \hat{u}) dy \quad [9]$$

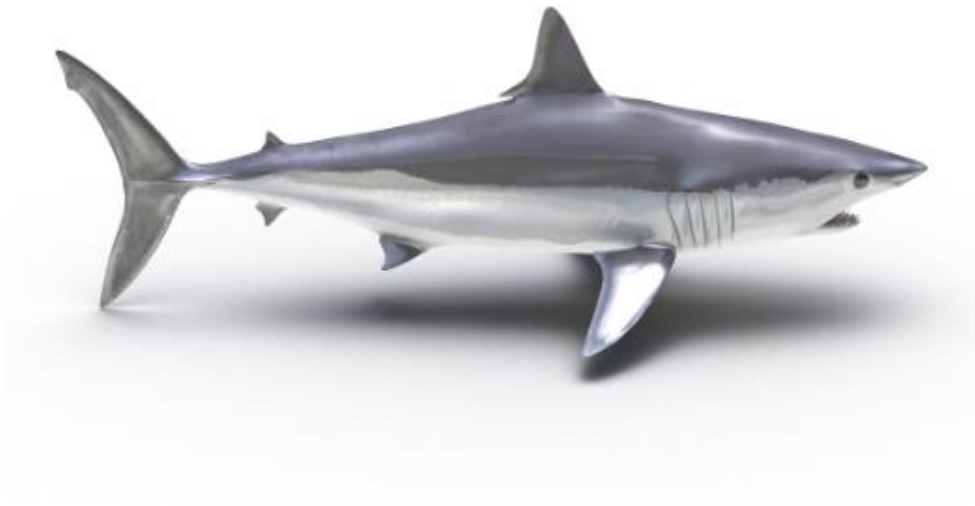
where  $\hat{u}$  is the phase-averaged streamwise velocity (Goett, 1939; Taylor et al., 2010). The total drag was obtained by multiplying this sectional drag with the span of the caudal fin, which was 15 cm for the lunate and 10.5 cm for the heterocercal caudal fins. To compare results between this study and others, the drag force is expressed as the coefficient of drag ( $C_D$ ):

$$C_D = \frac{DW}{\frac{1}{2}\rho u_\infty^2 W_A} \quad [10]$$

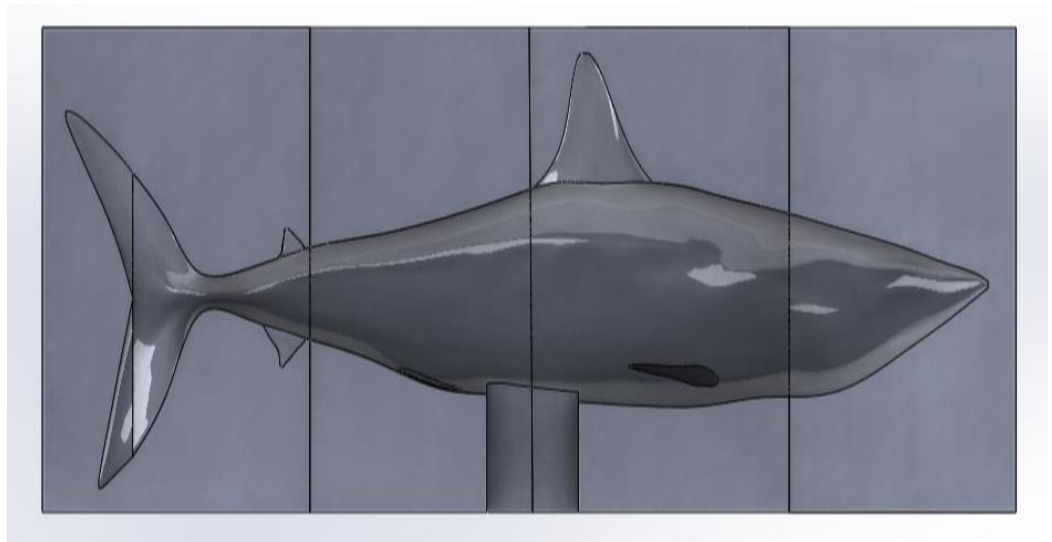
where  $\rho$  is the density of water, and  $W_A$  is the wetted area of the model, that is the surface area in contact with the water (Alexander, 1990; Sagong et al., 2013). This surface area was estimated from the CAD drawing of the Shortfin Mako model (Sagong et al., 2013).

Table 1: Summary of conducted experiments and associated parameters. All the experiments were performed in a water depth of 0.38m and flow speed of  $\sim 0.2\text{m/s}$ .

Caudal Fin Morphology	Measurement Location	PIV Plane	Model Total Length (cm)	Caudal Oscillation Frequency (Hz)	Flow Velocity (m/s)	Aspect Ratio
Lunate	Upper lobe	(x, y)	50	0.40	0.20	3.75
	Fork	(x, y)				
	Span	(x, z)				
Heterocercal	Upper lobe	(x, y)	56	0.40	0.20	2.1
	Fork	(x, y)				
	Span	(x, z)				



*Figure 6: Figure 6: Shortfin Mako 3D drawing (TurboSquid.com) used to create the mold.*



*Figure 7: Schematic of the Shortfin Mako mold, i.e., the negative of the Shortfin Mako drawing in Figure 6, where the vertical black lines indicate the different sections of the mold that were printed separately.*

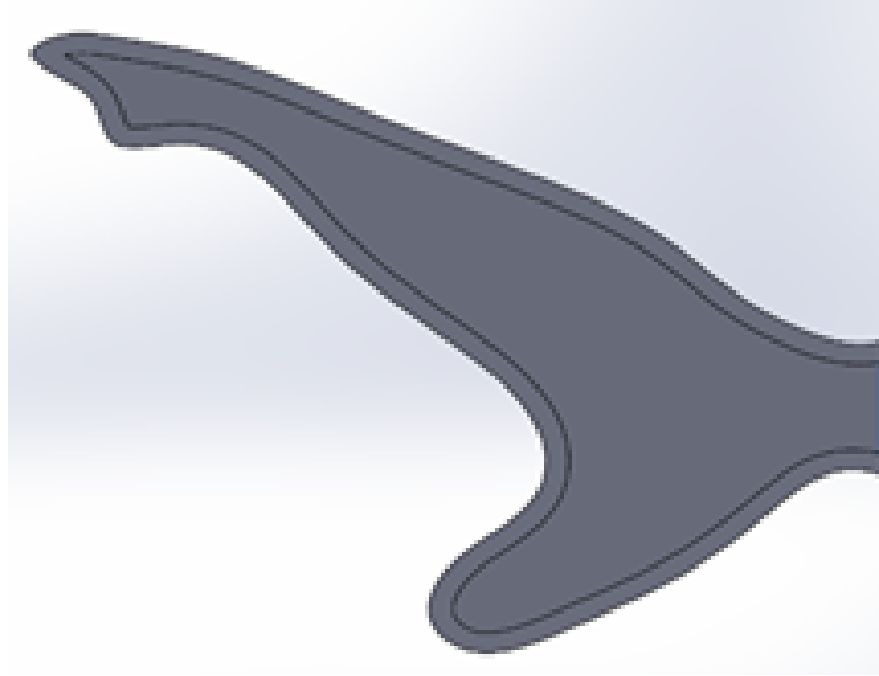


*Figure 8: Line drawing of the mold of the heterocercal caudal fin morphology investigated in this experiment, modeled after a Blacktip Shark (*Carcharhinus limbatus*).*

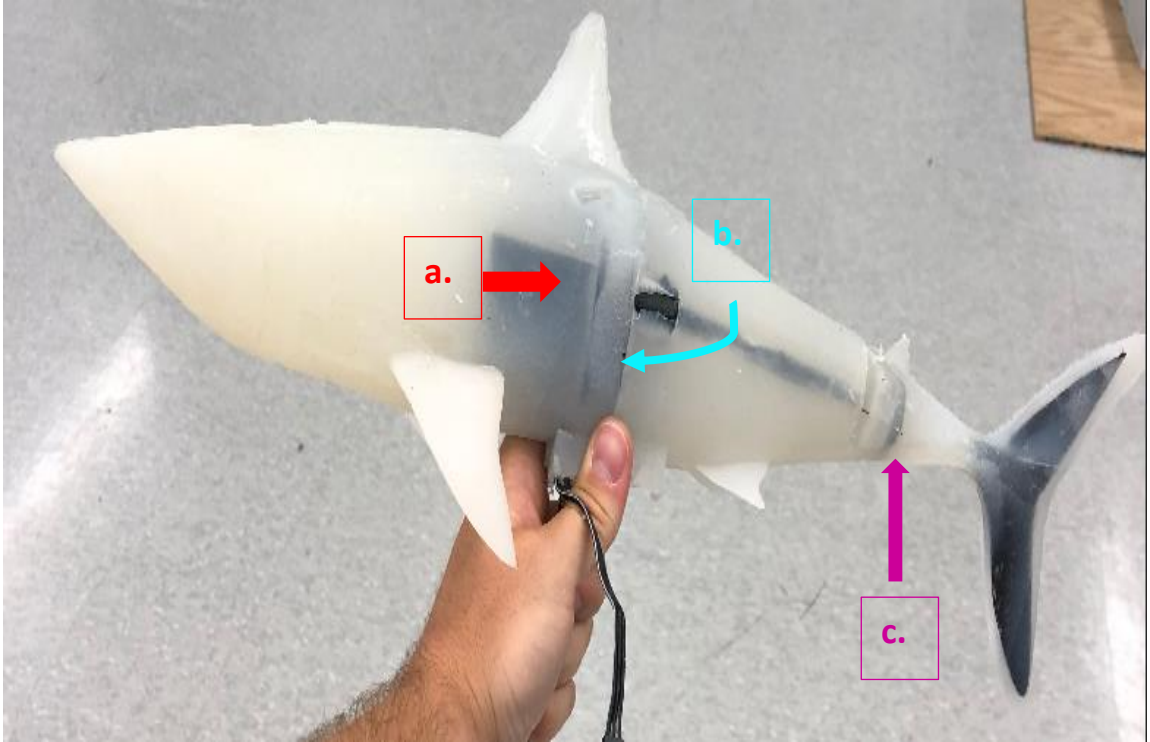


*Figure 9: Image of the silicone shark model with the lunate caudal fin morphology attached. a. Protective housing surrounding the servo motor. b. Support plate which anchors the model. c. Swim plate which allows the caudal fin to oscillate.*

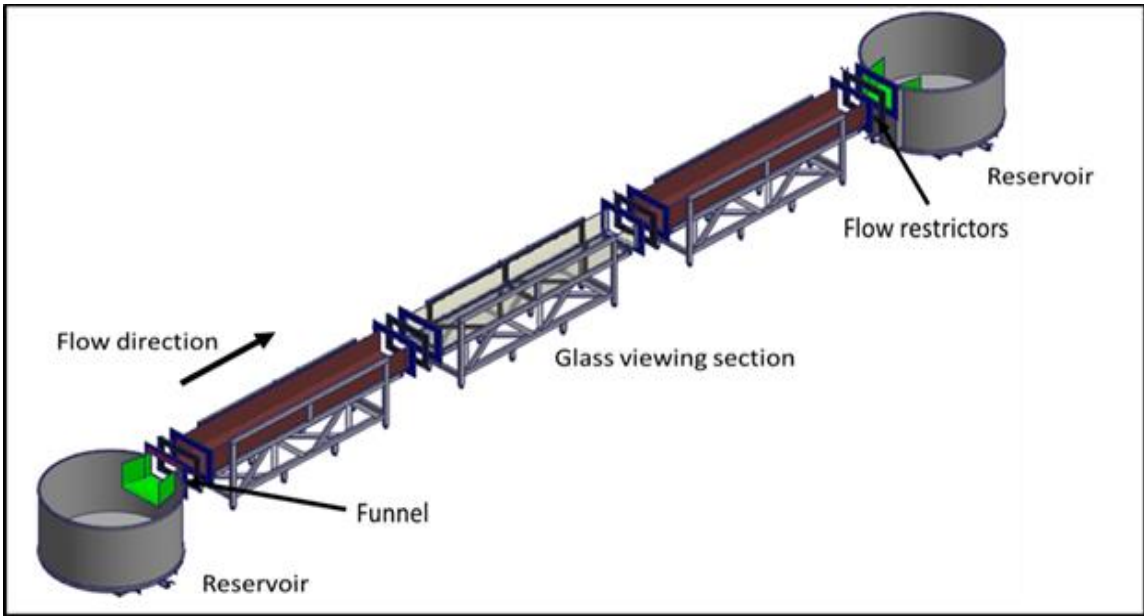


Figure 10: Isometric rendering of the flume. Courtesy of Jerry Quick.



*Figure 11: The Shortfin Mako model positioned in the flume with the laser illuminating the streamwise-spanwise ( $x, y$ ) plane behind the fork of the lunate caudal fin.*

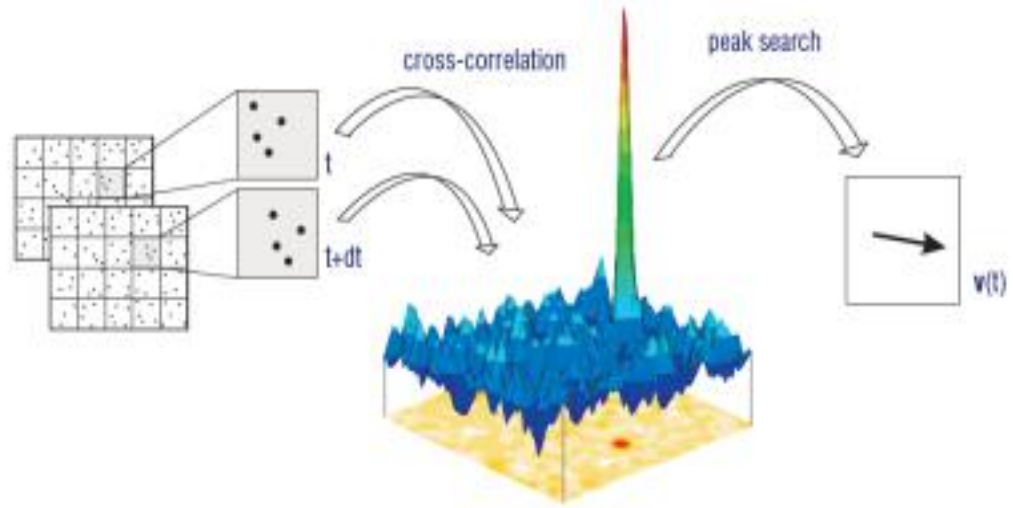


Figure 12: Schematic of the cross-correlation process used in PIV analysis. From Wieneke, (2017).

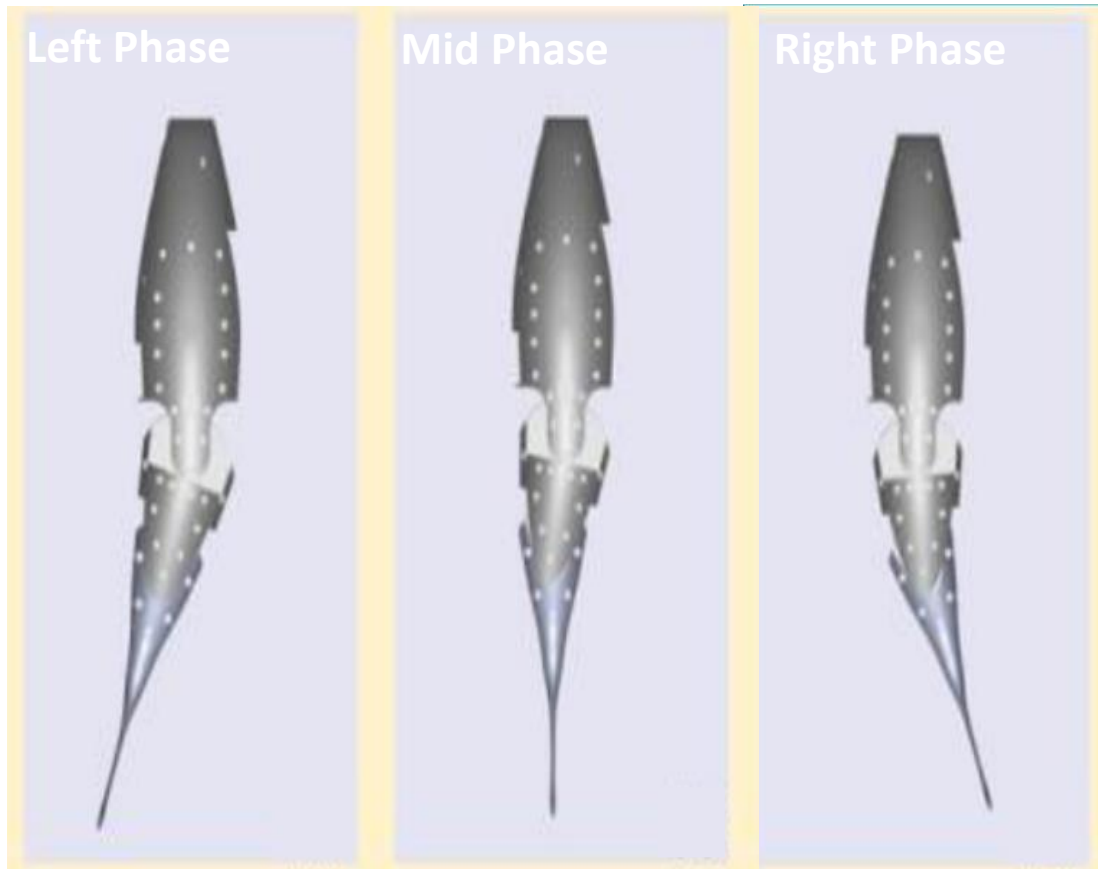


Figure 13: Image showing the phases used during this experiment. The left and right phases were used for the streamwise-spanwise plane, and the mid phase for the streamwise-normal plane. Based-on image from Ay et al., (2018).

## 5.0 Results

Phase averaged wake characteristics and hydrodynamic forces behind each of the oscillating caudal fin morphologies at all PIV measurement plane locations are discussed in this section. The results allow for a detailed examination of the wake characteristics and hydrodynamic forces generated by the two distinct caudal fin morphologies when paired with steady thunniform swimming; thereby providing information on the effect caudal fin morphology has on the hydrodynamic performance of the Shortfin Mako. The first subsection discusses wake characteristics and the second subsection discusses the hydrodynamic forces.

### 5.1 Wake Characteristics

We chose to show only the characteristics of the left phase of each morphology in the streamwise-spanwise plane due to the similarity in results between the two phases investigated. Results from the streamwise-normal (or span) plane are for the phase of the tail beat where the caudal fin is directly behind the model.

Figure 14 presents the magnitude of the phase averaged streamwise velocity,  $\hat{u}$ . In each measured PIV plane, a velocity deficit appears in the wake for both morphologies. The lowest velocity can be seen at small  $x$ -positions, directly behind the caudal fin. The velocity field does not recover to the free stream value at any measured  $x$ -position within the wake in the FOV but it does generally increase as the streamwise distance from the caudal fin increases. Measurements taken at the upper lobe for each morphology show the smallest velocity decrease, with the velocity only decreasing  $\sim 0.04$  m/s, which is possibly due to the small local length. Local length

refers to the distance between the leading and trailing edges of the fin for each PIV measurement plane (for both morphologies). The local length is the smallest at the upper lobe of the lunate morphology, at 0.012 m. The overall similarity in the size and velocity magnitude for each PIV measurement plane suggests that the wake is not significantly affected by the change in caudal fin morphology.

In Figure 15, contours of  $\widehat{\omega}_z$  and  $\widehat{\omega}_y$  from the respective measured PIV plane are presented. We observe a region of positive vorticity, above a region of negative vorticity behind the caudal fin. The presence of two regions of opposing vorticity signs in such an arrangement shows that the oscillating caudal fin is generating two distinct shear layers (Williamson and Roshko, 1988), suggesting that each morphology could be propulsive. The upper lobe of each morphology generates the smallest regions of concentrated vorticity in terms of the width of the shear layers, possibly due to the small local length. The shear layers at this location however appear to be the largest in terms of magnitude, which may have been a result of this portion of the caudal fin being exposed directly to the free stream, results at the fork and span PIV measurement planes may have been affected by the main body of the model which may have interacted with the flow, possibly slowing it down. Phase averaged normal vorticity measured at the fork was similar for each phase and morphology. Measured phase averaged spanwise vorticity from the streamwise-normal PIV plane was lower in magnitude and less organized relative to the upper lobe and fork locations, possibly due to the FOV being farther away from the trailing edge of the caudal fin, or due to the center phase of these measurements. The additional downstream distance allows for dissipation of some of the turbulence by viscous forces, which could result in decreasing vorticity magnitudes. Vorticity is shown to dissipate as the streamwise distance from the caudal fin increases for each measured PIV plane, also due to viscous forces.

Distributions of phase averaged Reynolds shear stress generated by each morphology are presented in Figure 16. Areas with non-zero stress indicate the presence of turbulence. The regions of higher Reynolds shear stress indicate areas of high momentum transfer, which is consistent with what is expected in turbulent shear flows (Pope, 2001). While areas outside the wake show approximately zero Reynolds shear stress because of little fluctuating velocity. Reynolds stresses at the upper lobe of both morphologies are smaller than at the fork, most likely due to the small local length at the upper lobe PIV measurement plane. Reynolds stresses at the fork are the largest presumably because of the larger local length at the PIV measurement location, which are 4 and 5 cm for the lunate at heterocercal morphologies respectively. The Reynolds stresses for the heterocercal caudal fin in the streamwise-normal PIV plane are similar to that of the lunate morphology. For all measured PIV planes, as the streamwise distance from the caudal fin increases, the Reynolds shear stresses decrease due to viscous forces dissipating available kinetic energy and therefore decreasing momentum transfer.

Figure 17 presents contours of the phase averaged TKE in each measured PIV plane for both morphologies. The upper lobe and fork locations (streamwise-spanwise plane) generate the most TKE, while the measurements in the span plane are shown to be the lowest. For measurements taken in the streamwise-spanwise plane, this result is presumably due to differences in local length. Each measured PIV plane shows highest levels of TKE closest to the caudal fin, and as  $x$  increases, TKE decreases. This result is again due to viscous forces reducing the available energy while a source of energy is no longer present. This effect may be seen the clearest at the mid position as the FOV was farther from the trailing edge than other locations. The areas outside of the wake show low levels of TKE because of lower levels of fluctuating velocity in the freestream.

The similarity in the wake characteristics examined thus far suggest that caudal fin morphology when paired with thunniform oscillations does not affect these hydrodynamic characteristics at these  $Re$ .

### 5.1.1 Spectra

Fluctuating streamwise velocity energy spectra were calculated according to Section 4.5.4 and are presented in Figure 18. These spectra are of the fluctuating streamwise velocity component ( $u'$ ) in the streamwise, spanwise, and normal directions. Our results indicate the presence of an inertial subrange in each measured PIV plane, as each spectrum reasonably follows the  $-5/3$  scaling law for a range of wavenumbers (spatial frequency of a wave), however, there does not appear to be a clear separation of scales which is a consequence of the low  $Re$  of this study (Pope, 2001). This trend is consistent for fluctuating streamwise velocity spectra computed along the streamwise and spanwise directions (Figure 18a, and 18b), as well as that computed along the streamwise and normal directions (Figure 18c). An inertial subrange lies between the production and dissipation scales, this subrange is where energy is transferred from larger to smaller eddies without loss of energy. The presence of an inertial subrange indicates that there is scale separation between larger energy containing eddies and dissipation-scale eddies. These velocity spectra are similar across morphologies, and all spectra follow the same general trend, with energy decreasing as wavenumber ( $k$ ) increases ( $k_1$ ,  $k_2$ , and  $k_3$  represent wavenumber in each direction, respectively). This result indicates that both morphologies impart similar levels of translational kinetic energy at all scales into their respective wakes.

Spectra of the fluctuating normal and spanwise vorticity components were similarly calculated along the streamwise, spanwise, and normal directions, according to Section 4.5.4 and are presented in Figure 19. Energy levels between the lunate and heterocercal morphologies are shown to differ by a factor of approximately 2 in both directions over all scales, at the upper and

fork locations, indicating that the lunate morphology imparts greater amounts of rotational kinetic energy into the wake at all scales at the rightmost and leftmost excursions of the caudal fin. In contrast, the differences in these spectra between the morphologies measured in the span planes is less pronounced but the lunate still imparts higher energy levels. This difference may be because the fluctuating normal vorticity is impacted more by the change in the caudal fin morphology than the fluctuating spanwise vorticity, or, another possible reason may be that as the caudal fin reaches its leftmost/rightmost later excursion it sheds more vorticity as the caudal fin changes direction. This shedding may be what is captured at the upper and fork PIV measurement planes, and may be different between the two morphologies. The enhanced spectral energy of the lunate caudal fin might suggest that the wake is more organized behind the lunate morphology because of the symmetry of the epichordal and hypochordal lobes; such organization may promote more efficient energy transfer within the wake. This result is consistent with previous studies, in which the vortices generated by an oscillating lunate caudal fin were found to be more concentrated and contain more energy than other tested morphologies (Liu and Dong, 2016; Han et al., 2017). This result indicates that the trailing edge shape may be the dominant factor when considering the amount of rotational kinetic energy imparted to the flow at these  $Re$ .

## 5.2 Hydrodynamic Forces

In the current study, the sectional drag coefficient for each phase, morphology, and PIV measurement plane was estimated using the wake velocity deficit method presented in Section 4.5.5. The momentum deficit profiles used for these calculations are presented in Figure 20. The black lines in Figure 14 enclose the streamwise region over which the velocity profiles were spatially averaged over the streamwise direction in addition to the ensemble phase averaging. The momentum deficit profiles measured at the span PIV plane were extrapolated because the

velocity deficit did not recover back to zero within the FOV; not accounting for this issue would generate inaccurate results. Figures 14c and 14f illustrate this issue, and show that free stream velocities are only encountered at the top portion of the region over which the velocity profiles were averaged in the span PIV measurement plane.

Drag coefficient results from the fork of the lunate morphology were the highest at 0.02. The drag coefficients calculated in the span plane were the same for each morphology at 0.01. Differences between the magnitudes of the deficits between phases of the lunate morphology at the upper lobe (Figure 20a) may be explained by the unsteady oscillatory motion of the fin. The fin may have moved slightly out of plane when oscillating to the right, altering the 0.012 m local length, resulting in a smaller momentum deficit. Drag coefficient results were smaller for the lunate morphology at the upper lobe location than the hetero, but vice versa measured at the fork location. At the fork location, the momentum deficit was wider for the lunate morphology, approximately 0.10 m, while the width of the momentum deficit for the hetero morphology was approximately 0.08 m. This difference may have been because the width of the lunate morphology at the fork in the spanwise direction was greater than that of the heterocercal morphology at the same location, 0.013 and 0.007 m respectively. This additional width may have altered the trailing edge of the lunate morphology such that it became more like a bluff body relative to the hetero morphology, which was more streamlined, resulting in an increased drag force acting on the lunate morphology. The overall similarities in our results, which are easily seen in Figure 21, suggest that caudal fin morphology does not have an effect on the drag experienced by the Shortfin Mako at these  $Re$ . This result is also reflected in the similarity of the left and mid phase momentum deficit profiles (Figure 20) and drag coefficient results (Table 2). The drag coefficient results are consistent with those from previously conducted studies on similar species (Tamura and Takagi, 2008; Sagong et al., 2013; Takagi et al., 2013). The drag coefficient results in

the span plane and at the fork of the heterocercal morphology were most similar to results in the literature – see Table 2.

Table 2: Measured PIV planes and morphologies along with associated fin parameters phase, local Re, free stream velocity, and,  $C_D$ . Results from previous experiments are also listed in the table - Tamura and Takagi, (2008)<sup>1</sup>, Takagi et al., (2013)<sup>2</sup>, Sagong et al., (2013)<sup>3</sup>.

Morphology	Location	Phase	Local Length (m)	Local Re	$U_\infty$ (m/s)	$C_D$
Lunate	Upper	Left	0.012	$2.76 \times 10^3$	0.234	0.010
Lunate	Upper	Right	0.012	$2.76 \times 10^3$	0.232	0.006
Lunate	Fork	Left	0.040	$9.24 \times 10^3$	0.231	0.020
Lunate	Fork	Right	0.040	$9.28 \times 10^3$	0.232	0.020
Lunate	Span	Mid	0.040	$8.80 \times 10^3$	0.222	0.010
Hetero	Upper	Left	0.026	$5.72 \times 10^3$	0.225	0.006
Hetero	Upper	Right	0.026	$5.72 \times 10^3$	0.224	0.006
Hetero	Fork	Left	0.050	$1.15 \times 10^4$	0.231	0.010
Hetero	Fork	Right	0.050	$1.13 \times 10^4$	0.227	0.010
Hetero	Span	Mid	0.050	$1.12 \times 10^4$	0.225	0.010
Lunate <sup>1</sup>	Span	Mid	0.040	$3.00 \times 10^4$	0.750	0.010
Lunate <sup>2</sup>	Span	Mid	0.040	$2.40 \times 10^4$	0.600	0.010
Lunate <sup>3</sup>	Span	Mid	0.10	$2.00 \times 10^6$	2.00	0.009

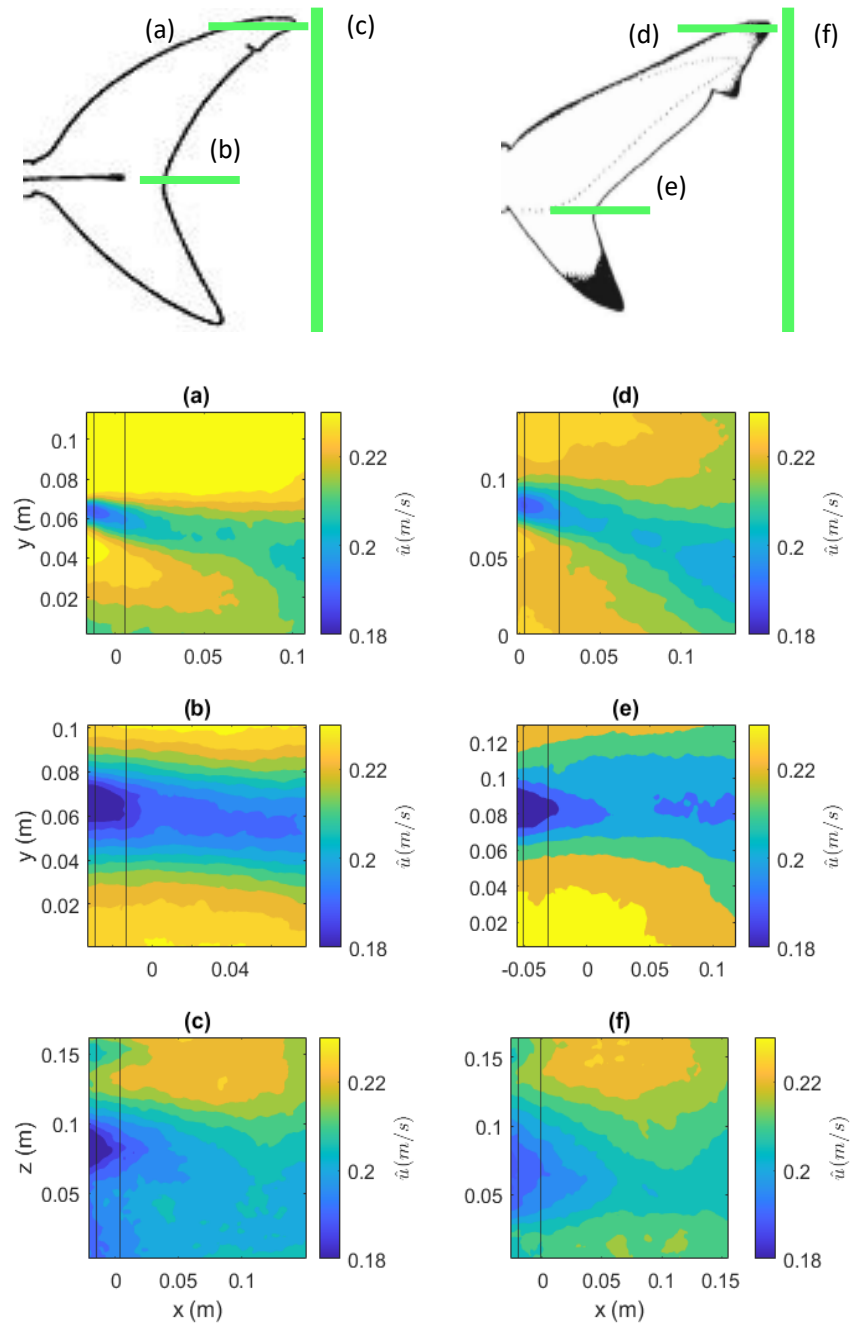


Figure 14: Contours of the left and mid phase of the streamwise velocity components for each morphology. Subplots a, b, and c show the upper, fork, and span measurement planes for the lunate morphology, and subplots d, e, and f show the upper, fork and span PIV measurement planes of the heterocercal morphology. The panel at the top shows the PIV measurement plane locations for reference, labelled by their corresponding subfigure letter.

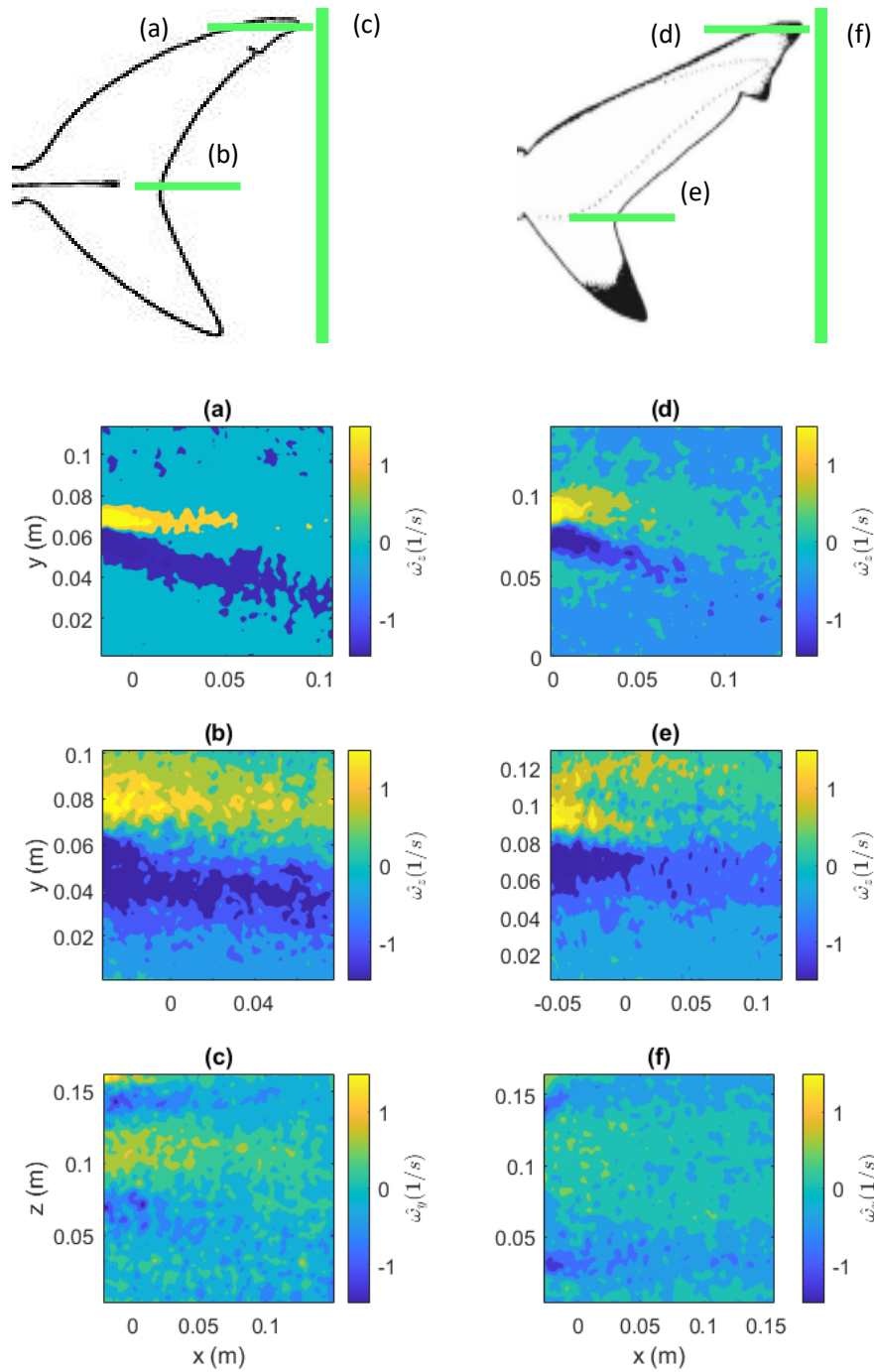


Figure 15: Contours of the left and mid phase normal and spanwise vorticity components for each morphology. Subplots a, b, and c show the upper, fork, and streamwise PIV measurement planes of the lunate morphology, and subplots d, e, and f show the upper, fork, and span PIV measurement planes of the heterocercal morphology. The panel at the tops shows the PIV measurement plane locations for reference, labelled by their corresponding subfigure letter.

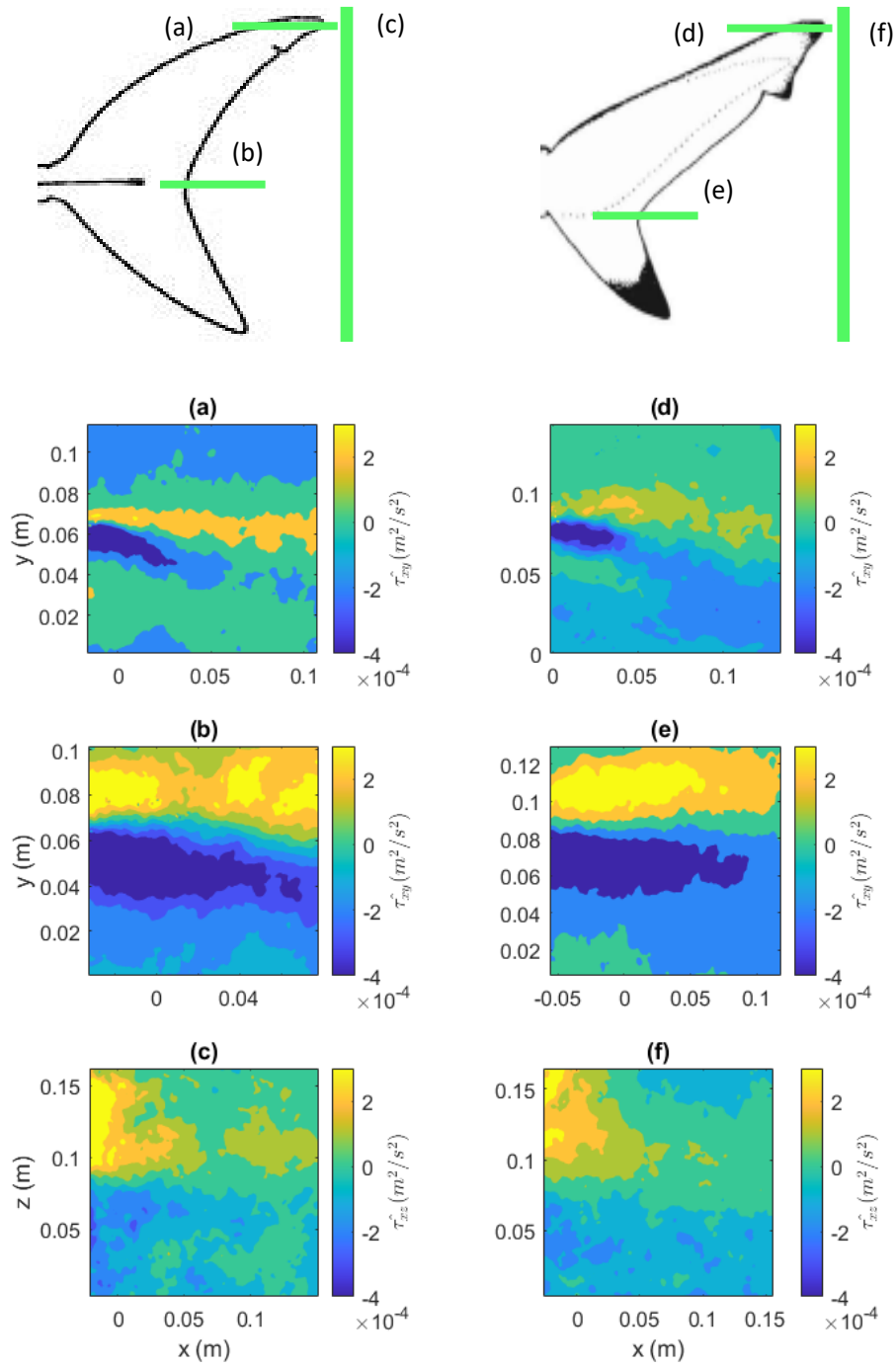


Figure 16: Contours of the left and mid phase Reynolds shear stresses for each morphology. Subplots a, b, and c show the upper, fork, and span PIV measurement planes of the lunate morphology, and subplots d, e, and f show the upper, fork, and span PIV measurement planes of the hetero morphology. The panel at the top shows the PIV measurement plane locations for reference, labelled by their corresponding subfigure letter.

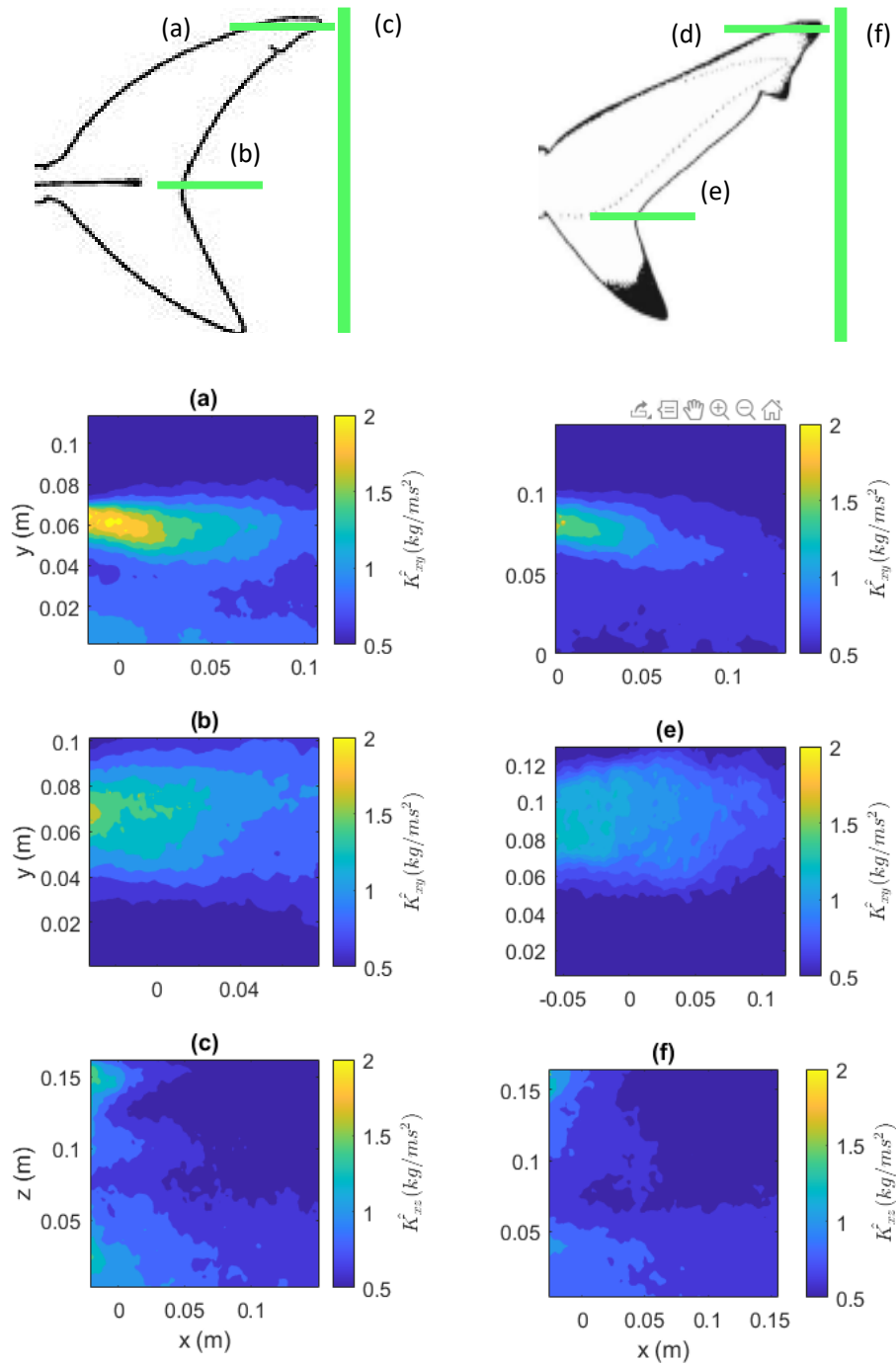


Figure 17: Phase averaged TKE for the left and mid phase for each morphology. Subplots a, b, and c show the upper, fork, and span PIV measurement planes of the lunate morphology, and subplots d, e, and f show the upper, fork, and span PIV measurement planes of the heterocercal morphology. The panel at the top shows the PIV measurement plane locations for reference, labelled by their corresponding subfigure letter.

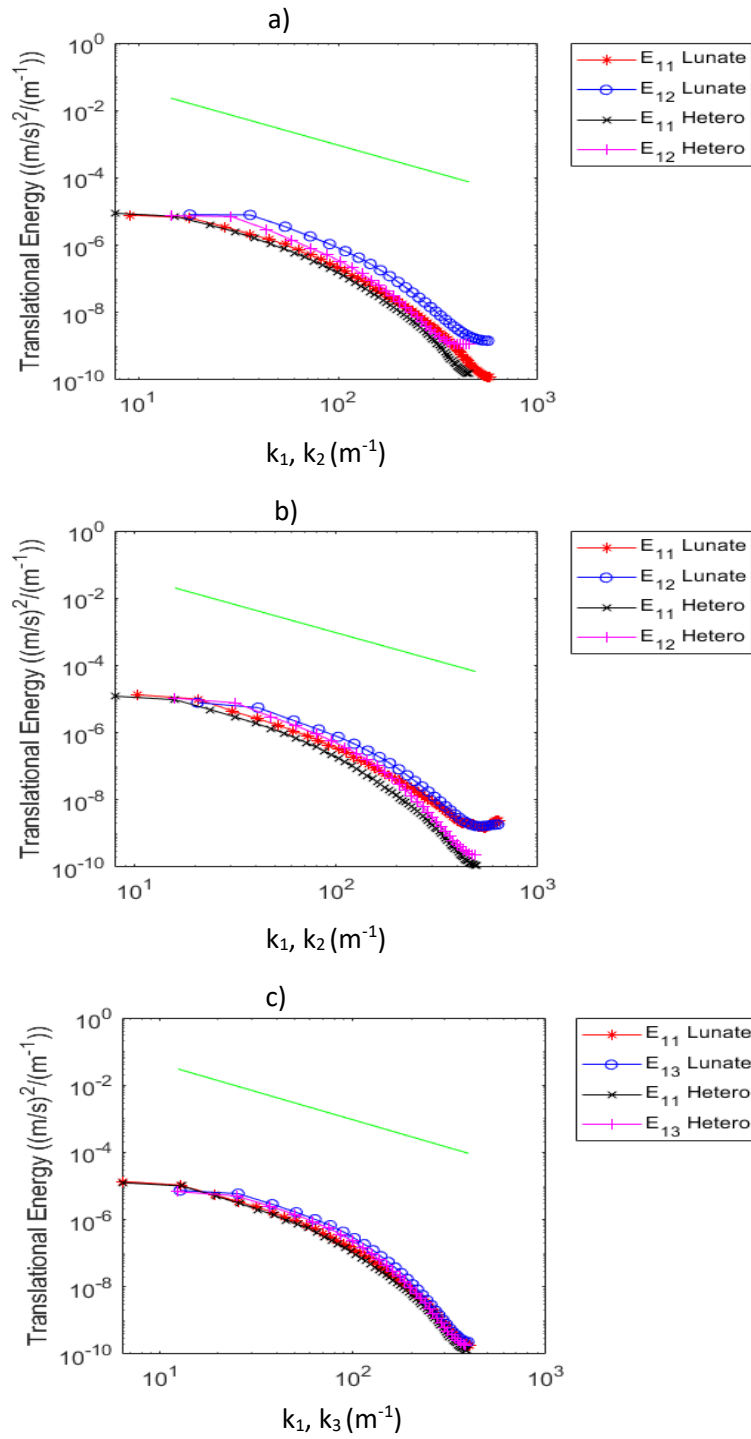


Figure 18: Fluctuating streamwise velocity spectra in the streamwise, spanwise, and normal directions from data measured at the upper and fork PIV measurement planes respectively. Subplot c shows spectra computed along the streamwise and normal directions for data measured at the span PIV measurement plane. The green line represents the  $k^{-5/3}$  power law for turbulence in the inertial range.

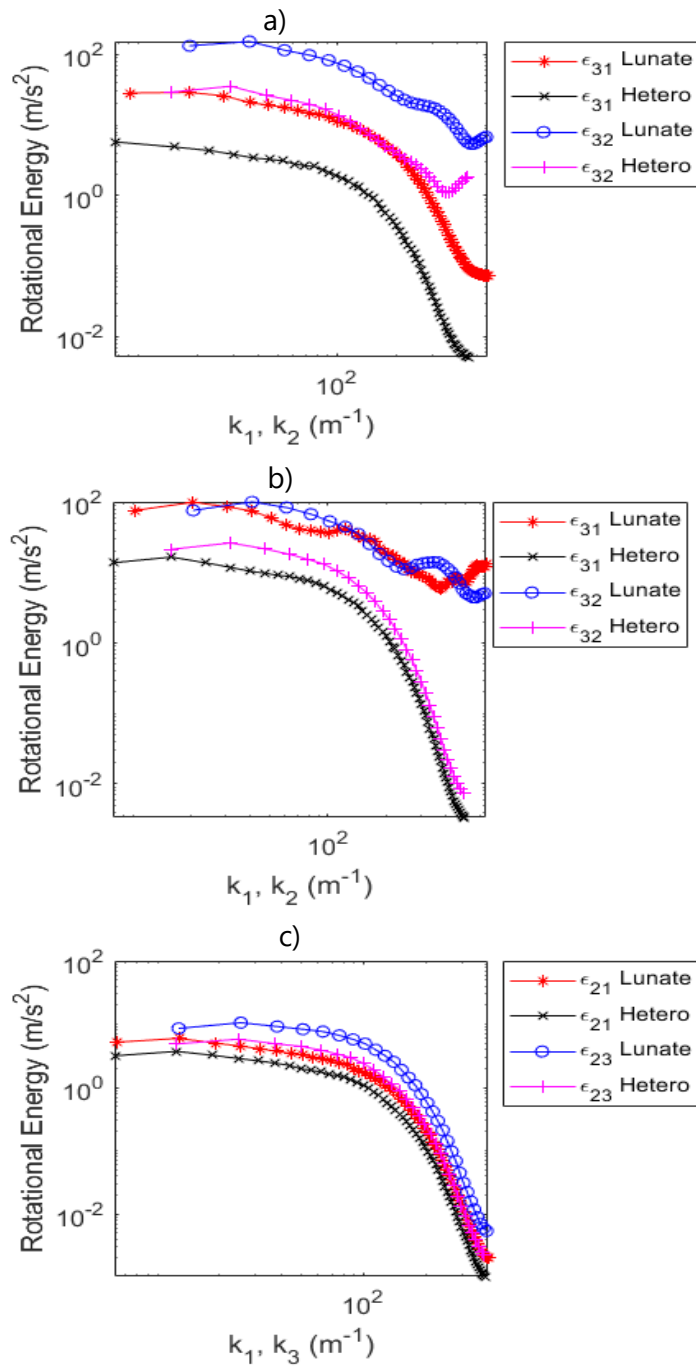


Figure 19: Phase averaged fluctuating normal and spanwise vorticity spectra along the streamwise, normal, and spanwise directions. Subplots a and b show fluctuating normal vorticity spectra computed along the streamwise and spanwise directions from data measured at the upper and fork PIV measurement planes respectively. Subplot c shows fluctuating spanwise vorticity spectra computed along the streamwise and normal directions for data measured at the span PIV measurement plane.

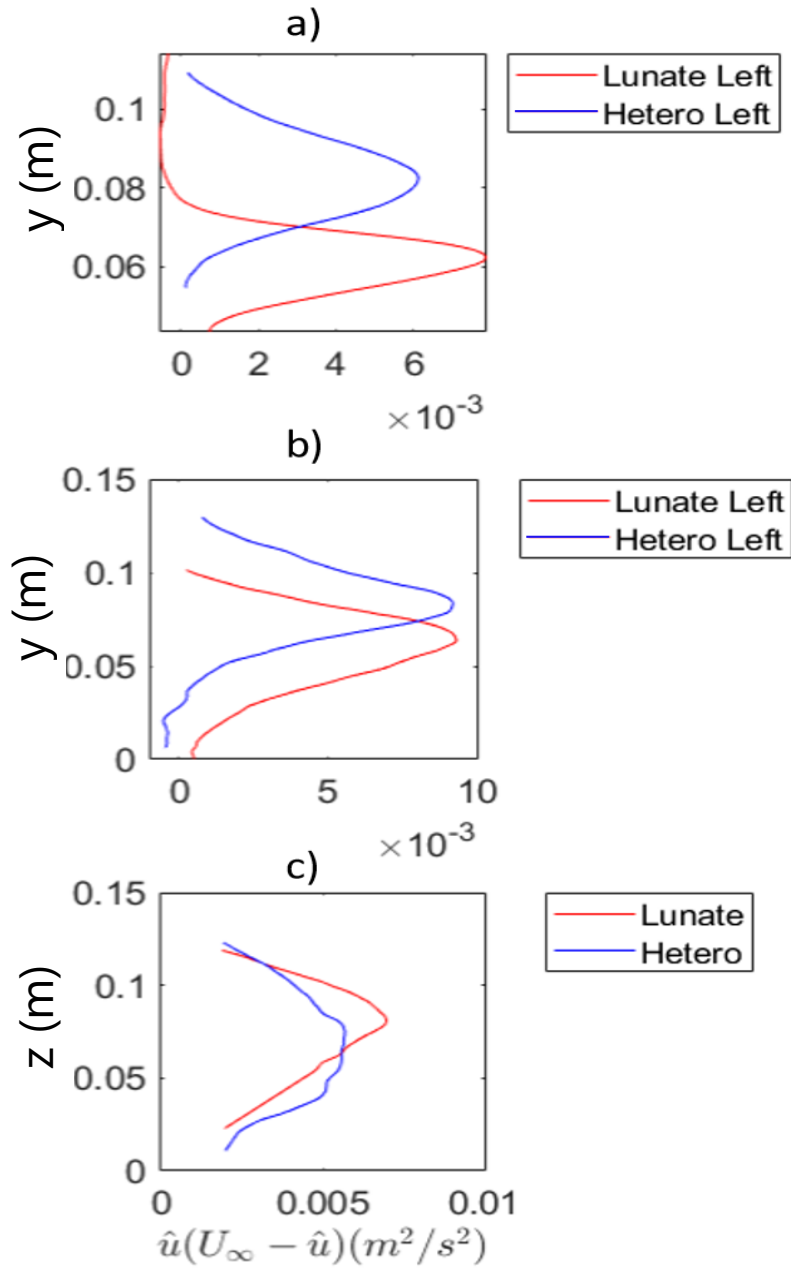


Figure 20: Phase-averaged momentum deficit (a, b) spanwise and (c) normal profiles in the wake behind an oscillating Shortfin Mako model. Velocities are phase-averaged and averaged over the streamwise direction between the two vertical black lines shown in Figure 14. Subplots a, b, and c are of the upper, fork, and span PIV measurement plane respectively.

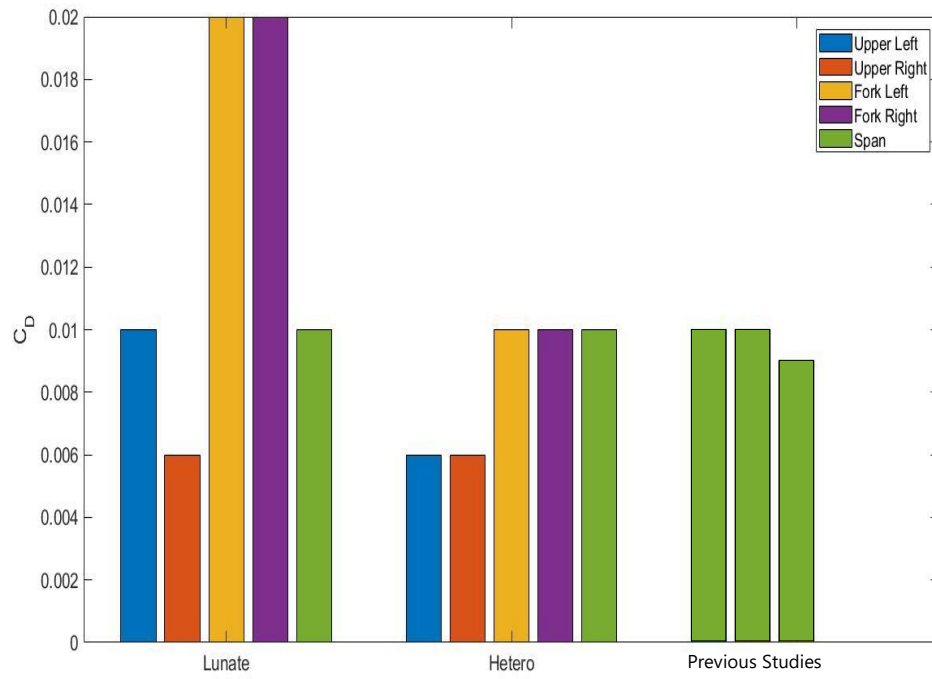


Figure 21: Bar chart showing the CD of both morphologies at each PIV measurement plane, as well as those from previous studies listed in the order they appear in Table 2.

## 6.0 Summary and Conclusions

In this study, we set out to further our understanding of shark hydromechanics, specifically the pairing of thunniform oscillations and caudal fin morphology of the Shortfin Mako shark. To this end, we i) evaluated the wake characteristics behind an oscillating Shortfin Mako shark with two separate caudal fin morphologies, in 3 different measurement planes and ii) investigated the effect caudal fin morphology has on drag.

Results of the flow characteristics behind each of the two morphologies used in our flow experiments demonstrate that the trailing edge shape has little effect on the wake characteristics at these Reynolds numbers, except for the fluctuating vorticity spectra. Similar values of each calculated hydrodynamic characteristic and drag coefficients were seen at each measurement plane for both morphologies. However, results showed that the fluctuating vorticity spectra contained more energy in the wake behind the lunate caudal fin compared to the heterocercal caudal fin at all length scales examined, suggesting that the trailing edge shape influences the amount of rotational kinetic energy that the caudal fin imparts into the wake, with the lunate caudal fin imparting higher levels of fluctuating normal vorticity, especially at the leftmost and rightmost excursions of the caudal fin. The hydrodynamic forces were also similar for each measurement plane and were similar to values calculated in previous studies. Lowest levels of each calculated quantity were seen at the upper lobe of both morphologies, which presumably result from the small local length scale at the upper lobe. The highest levels of each calculated

quantity were seen at the fork location, again presumably, because of the larger local length scale at the fork.

These results, raise questions about the selective pressure that led to the evolution of such a specialized structure as a lunate caudal fin in a group in which most species utilize a more asymmetrical tail. Other hydrodynamic characteristics such as acceleration, lift, or stability, none of which were examined in this study, may play a significantly more beneficial role in evolution of the lunate morphology (than the heterocercal). For example, this possibility is supported by previous research conducted using Bottlenose dolphins, which also perform thunniform oscillations utilizing a lunate caudal fin albeit rotated 90° to that of the Shortfin Mako, that found that the limited lateral oscillations of the anterior part of the body increased stability while cruising (Fish et al., 2000). This finding may indicate that those organisms utilizing other swimming modes are more unstable because of the increased amount of lateral movement at the anterior of the organism. Another possible selective pressure not examined during this experiment was the flexibility of each caudal fin morphology. The heterocercal morphology was more rigid in this study than what can be expected in nature (relative to the lunate morphology) and may have altered the hydrodynamic of the heterocercal morphology such that it became more similar to the lunate morphology in terms of hydrodynamic performance; future studies should investigate how this difference in flexibility of the tail might impact hydrodynamic characteristics. For example, this increased rigidity of the heterocercal morphology may have decreased the amount of recoil acting on it as the fin oscillated, thus decreasing the amount of energy it may have imparted to the flow. Similarly, the degradation in operational quality of the servo motor within our models may have been a source of error by causing the caudal fin to oscillate unnaturally.

Despite possible shortcomings and anatomical inconsistencies, this study represents a significant advancement in understanding thunniform swimming and the effect of caudal fin

morphology on the hydrodynamic characteristics of Shortfin Mako sharks. Our results were shown to be consistent with those results of previous studies and could be a good starting point for future research on Shortfin Mako physiology or AUV engineering. Future AUVs or similar biomimetic models operating at similar Reynolds numbers may choose to focus on better mimicking the thunniform motion of the Shortfin Mako, rather than the shape of any derived propulsor. This advancement may allow these technologies to move through the aquatic medium at lower operating costs than traditional rotating propellers (Mazlan, 2015).

We conclude that caudal fin morphology when paired with thunniform oscillations does not significantly influence the hydrodynamic characteristics or force characteristics of the Shortfin Mako shark at the range of Re numbers examined, except for the fluctuating vorticity. Future research should focus on improving the mechanical operation and design of any oscillating Shortfin Mako models, as well as creating a flow regime more closely in line with what is expected in nature to possibly improve the accuracy of results.

## 7.0 References

- Adaramola, M. S., Akinlade, O. G., Sumner, D., Bergstrom, D. J., & Schenstead, A. J. (2006). Turbulent wake of a finite circular cylinder of small aspect ratio. *Journal of Fluids and Structures*, 22(6-7), 919-928.
- Adrian, R. J. (1986). Image shifting technique to resolve directional ambiguity in double-pulsed velocimetry. *Applied Optics*, 25(21), 3855-3858.
- Adrian, R. J. (1991). Particle-imaging techniques for experimental fluid mechanics. *Annual review of fluid mechanics*, 23(1), 261-304.
- Adrian, L., Adrian, R. J., & Westerweel, J. (2011). *Particle image velocimetry* (No. 30). Cambridge university press.
- Afroz, F., Lang, A., Habegger, M. L., Motta, P., & Hueter, R. (2016). Experimental study of laminar and turbulent boundary layer separation control of shark skin. *Bioinspiration & biomimetics*, 12(1), 016009.
- Akanyeti, O., Putney, J., Yanagitsuru, Y. R., Lauder, G. V., Stewart, W. J., & Liao, J. C. (2017). Accelerating fishes increase propulsive efficiency by modulating vortex ring geometry. *Proceedings of the National Academy of Sciences*, 114(52), 13828-13833.
- Anderson Jr, J. D. (2010). Fundamentals of aerodynamics. Tata McGraw-Hill Education.
- Anderson, J. M. (1996). Vorticity Control for Efficient Propulsion. Massachusetts Inst of Tech Cambridge.

- Bao, Y., & Tao, J. J. (2014). Dynamic reactions of a free-pitching foil to the reverse Kármán vortices. *Physics of Fluids*, 26(3), 031704.
- Bernal, D., Dickson, K. A., Shadwick, R. E., & Graham, J. B. (2001). Analysis of the evolutionary convergence for high performance swimming in lamnid sharks and tunas. *Comparative Biochemistry and Physiology Part A: Molecular & Integrative Physiology*, 129(2-3), 695-726.
- Bone, Q. (1978). Locomotor muscle. *Fish physiology*, 7, 361-424.
- Breder Jr, C. M. (1926). The locomotion of fishes. *Zoologica*, 4, 159-291.
- Brooks, S. A., & Green, M. A. (2019). Experimental study of body-fin interaction and vortex dynamics generated by a two degree-of-freedom fish model. *Biomimetics*, 4(4), 67.
- Bushnell, D. M., & Moore, K. J. (1991). Drag reduction in nature. *Annual review of fluid mechanics*, 23(1), 65-79.
- Carey, F. G., & Teal, J. M. (1969). Mako and porbeagle: warm-bodied sharks. *Comparative Biochemistry and Physiology*, 28(1), 199-204.
- Çengel, Y. A., & Cimbala, J. M. (2006). Fluid mechanics: Fundamentals and applications. Boston: McGraw-Hill Higher Education.
- Cheng, H. K., & Murillo, L. E. (1984). Lunate-tail swimming propulsion as a problem of curved lifting line in unsteady flow. Part 1. Asymptotic theory. *Journal of Fluid Mechanics*, 143, 327-350.
- Chopra, M. G. (1976). Large widthtude lunate-tail theory of fish locomotion. *Journal of Fluid Mechanics*, 74(1), 161-182.

Chopra, M. G. (1974). Hydromechanics of lunate-tail swimming propulsion. *Journal of Fluid Mechanics*, 64(2), 375-392.

Chopra, M. G., & Kambe, T. (1977). Hydromechanics of lunate-tail swimming propulsion. Part 2. *Journal of Fluid Mechanics*, 79(1), 49-69.

Cohen, R. C. Z., & Cleary, P. W. (2010). Computational studies of the locomotion of dolphins and sharks using Smoothed Particle Hydrodynamics. In *6th World Congress of Biomechanics (WCB 2010). August 1-6, 2010 Singapore* (pp. 22-25). Springer, Berlin, Heidelberg.

Compagno, L. J. (2001). *Sharks of the world: an annotated and illustrated catalogue of shark species known to date* (No. 1). Food & Agriculture Org.

Crofts, S. B., Shehata, R., & Flammang, B. (2019). Flexibility of heterocercal tails: what can the functional morphology of shark tails tell us about ichthyosaur swimming?. *Integrative Organismal Biology*. 1(1), obz002.

Dewar, H., & Graham, J. (1994). Studies of tropical tuna swimming performance in a large water tunnel-kinematics. *Journal of Experimental Biology*, 192(1), 45-59.

Drucker, E. G., & Lauder, G. V. (2001). Locomotor function of the dorsal fin in teleost fishes: experimental analysis of wake forces in sunfish. *Journal of Experimental Biology*, 204(17), 2943-2958.

Du Clos, K. T., Lang, A., Devey, S., Motta, P. J., Habegger, M. L., & Gemmell, B. J. (2018). Passive bristling of mako shark scales in reversing flows. *Journal of The Royal Society Interface*, 15(147), 20180473.

Epps, B. P., y Alvarado, P. V., Youcef-Toumi, K., & Techet, A. H. (2009). Swimming performance of a biomimetic compliant fish-like robot. *Experiments in fluids*, 47(6), 927-939.

Flammang, B. E., & Lauder, G. V. (2009). Caudal fin shape modulation and control during acceleration, braking and backing maneuvers in bluegill sunfish, *Lepomis macrochirus*. *Journal of Experimental Biology*, 212(2), 277-286.

Flammang, B. E., Lauder, G. V., Tröolin, D. R., & Strand, T. (2011). Volumetric imaging of shark tail hydrodynamics reveals a three-dimensional dual-ring vortex wake structure. *Proceedings of the Royal Society B: Biological Sciences*, 278(1725), 3670-3678.

Fish, F. E. (1998). Imaginative solutions by marine organisms for drag reduction. In *Proceedings of the International Symposium on Seawater Drag Reduction* (Vol. 1, pp. 443-450). Newport, Rhode Island.

Fish, F. E., Peacock, J. E., & Rohr, J. (2000) Phase relationships between body components of odontocete cetaceans in relation to stability and propulsive mechanisms *Proc. 1st Int. Symp. on Aqua Bio-Mechanisms/International Seminar on Aqua Bio-Mechanisms (Tokai University Pacific Center, Honolulu, Hawaii)* ed N Kato and Y Suzuki pp 57-60

Fish, F., & Lauder, G. V. (2006). Passive and active flow control by swimming fishes and mammals. *Annu. Rev. Fluid Mech.*, 38, 193-224.

Gleiss, A. C., Potvin, J., & Goldbogen, J. A. (2017). Physical trade-offs shape the evolution of buoyancy control in sharks. *Proceedings of the Royal Society B: Biological Sciences*, 284(1866), 20171345.

Goett, H. J. (1939). *Experimental investigation of the momentum method for determining profile drag*. US Government Printing Office.

Gopalkrishnan, R., Triantafyllou, M. S., Triantafyllou, G. S., & Barrett, D. S. (1994). Active vorticity control in a shear flow using a flapping foil.

- Graham, J. B., Dewar, H., Lai, N. C., Lowell, W. R., & Arce, S. M. (1990). Aspects of shark swimming performance determined using a large water tunnel. *Journal of Experimental Biology*, 151(1), 175-192.
- Gray, J. (1953). Undulatory propulsion. *Journal of Cell Science*, 3(28), 551-578.
- Gui, L., Wereley, S. T., & Lee, S. Y. (2002, July). Digital filters for reducing background noise in micro PIV measurement. In *11th international symposium on the application of laser techniques to fluid mechanics, Lisbon*.
- Hackett, E. E., Luznik, L., Nayak, A. R., Katz, J., & Osborn, T. R. (2011). Field measurements of turbulence at an unstable interface between current and wave bottom boundary layers. *Journal of Geophysical Research: Oceans*, 116(C2).
- Han, P., Liu, G., & Dong, H. (2017). Proper orthogonal decomposition analysis on the hydrodynamic effects of the propulsor geometries in flapping propulsion. In *55th AIAA Aerospace Sciences Meeting* (p. 1708).
- Harding, L., Jackson, A., Barnett, A., Donohue, I., Halsey, L., Huveneers, C., Meyer, C., Papastamatiou, Y., Semmens, J. M., Spencer, E., Watanabe, Y., & Payne, N. (2021). Endothermy makes fishes faster but does not expand their thermal niche. *Functional Ecology*, 00, 1–9.
- Hong, C., & Chang-an, Z. (2005, July). Modeling the dynamics of biomimetic underwater robot fish. In *2005 IEEE International Conference on Robotics and Biomimetics-ROBIO* (pp. 478-483). IEEE.
- Josserand, C., Le Berre, M., Lehner, T., & Pomeau, Y. (2017). Turbulence: does energy cascade exist? *Journal of Statistical Physics*, 167(3-4), 596-625.

- Klimley, A. P., Beavers, S. C., Curtis, T. H., & Jorgensen, S. J. (2002). Movements and swimming behavior of three species of sharks in La Jolla Canyon, California. *Environmental biology of fishes*, 63(2), 117-135.
- Kulkarni, A. A., Patel, R. K., Friedman, C., & Leftwich, M. C. (2017). A robotic platform to study the foreflipper of the California sea lion. *Journal of visualized experiments: JoVE*, (119).
- Lauder, G. V. (2000). Function of the caudal fin during locomotion in fishes: kinematics, flow visualization, and evolutionary patterns. *American Zoologist*, 40(1), 101-122.
- Lauder, G. V., & Tytell, E. D. (2005). Hydrodynamics of undulatory propulsion. *Fish physiology*, 23, 425-468.
- Lee, J., Park, Y. J., Cho, K. J., Kim, D., & Kim, H. Y. (2017). Hydrodynamic advantages of a low aspect-ratio flapping foil. *Journal of Fluids and Structures*, 71, 70-77.
- Lighthill, M. J. (1960). Note on the swimming of slender fish. *Journal of fluid Mechanics*, 9(2), 305-317.
- Lighthill, M. J. (1969). Hydromechanics of aquatic animal propulsion. *Annual review of fluid mechanics*, 1(1), 413-446.
- Lighthill, M. J. (1970). Aquatic animal propulsion of high hydromechanical efficiency. *Journal of Fluid Mechanics*, 44(2), 265-301.
- Lighthill, S. J. (1975). *Mathematical biofluidynamics*. Society for Industrial and Applied Mathematics.
- Li, G. J., Luodin, Z. H. U., & Lu, X. Y. (2012). Numerical studies on locomotion performance of fish-like tail fins. *Journal of Hydrodynamics, Ser. B*, 24(4), 488-495.

Liu, G., & Dong, H. (2016). Effects of tail geometries on the performance and wake pattern in flapping propulsion. In *ASME 2016 Fluids Engineering Division Summer Meeting collocated with the ASME 2016 Heat Transfer Summer Conference and the ASME 2016 14th International Conference on Nanochannels, Microchannels, and Minichannels*. American Society of Mechanical Engineers Digital Collection.

Liu, G., Ren, Y., Dong, H., Akanyeti, O., Liao, J. C., & Lauder, G. V. (2017). Computational analysis of vortex dynamics and performance enhancement due to body-fin and fin-fin interactions in fish-like locomotion. *Journal of fluid mechanics*, 829, 65-88.

Marius, S. D., & Carmen-Anca, S. (2012). Fluid-structure interaction. *Fluid Dynamics, Computational Modelling and Applications*, 195-216.

Melling, A. (1997). Tracer particles and seeding for particle image velocimetry. *Measurement science and technology*, 8(12), 1406.

Mockett, C., Perrin, R., Reimann, T., Braza, M., & Thiele, F. (2010). Analysis of detached-eddy simulation for the flow around a circular cylinder with reference to PIV data. *Flow, turbulence and combustion*, 85(2), 167-180.

Moss, S. A. (1984). *Sharks: an introduction for the amateur naturalist*. Prentice Hall.

Müller, U. K., Van Den Heuvel, B. L. E., Stamhuis, E. J., & Videler, J. J. (1997). Fish foot prints: morphology and energetics of the wake behind a continuously swimming mullet (*Chelon labrosus* Risso). *Journal of Experimental Biology*, 200(22), 2893-2906.

Nogueira, J., Lecuona, A., & Rodriguez, P. A. (1997). Data validation, false vectors correction and derived magnitudes calculation on PIV data. *Measurement Science and Technology*, 8(12), 1493.

Pope, S. B. (2001). *Turbulent flows*.

- Raffel, M., Leiti, B., & Kompenhans, J. (1992). Data validation for particle image velocimetry. *Laser Techniques and Applications in Fluid Mechanics*, 210-226.
- Raffel, M., Willert, C. E., Scarano, F., Kähler, C. J., Wereley, S. T., & Kompenhans, J. (2018). *Particle image velocimetry: a practical guide*. Springer.
- Raspa, V., et al. "Vortex-induced drag and the role of aspect ratio in undulatory swimmers." *Physics of Fluids* 26.4 (2014): 041701.
- Reyier, E. A., Adams, D. H., & Lowers, R. H. (2008). First evidence of a high density nursery ground for the lemon shark, *Negaprion brevirostris*, near Cape Canaveral, Florida. *Florida Scientist*, 134-148.
- Reynolds, O. (1895). IV. On the dynamical theory of incompressible viscous fluids and the determination of the criterion. *Philosophical transactions of the royal society of london.(a.)*, (186), 123-164.
- Sagong, W., Jeon, W. P., & Choi, H. (2013). Hydrodynamic characteristics of the sailfish (*Istiophorus platypterus*) and swordfish (*Xiphias gladius*) in gliding postures at their cruise speeds. *PloS one*, 8(12), e81323.
- Sambilay Jr, V. C. (1990). Interrelationships between swimming speed, caudal fin aspect ratio and body length of fishes. *Fishbyte*, 8(3), 16-20.
- Sane, S. P. (2003). The aerodynamics of insect flight. *Journal of experimental biology*, 206(23), 4191-4208.
- Scarano, F. (2001). Iterative image deformation methods in PIV. *Measurement science and technology*, 13(1), R1.

Sepulveda, C. A., Kohin, S., Chan, C., Vetter, R., & Graham, J. B. (2004). Movement patterns, depth preferences, and stomach temperatures of free-swimming juvenile mako sharks, *Isurus oxyrinchus*, in the Southern California Bight. *Marine Biology*, *145*(1), 191-199.

Sepulveda, C. A., Graham, J. B., & Bernal, D. (2007). Aerobic metabolic rates of swimming juvenile mako sharks, *Isurus oxyrinchus*. *Marine Biology*, *152*(5), 1087-1094.

Schouveiler, L., Hover, F. S., & Triantafyllou, M. S. (2005). Performance of flapping foil propulsion. *Journal of fluids and structures*, *20*(7), 949-959.

Sfakiotakis, M., Lane, D. M., & Davies, J. B. C. (1999). Review of fish swimming modes for aquatic locomotion. *IEEE Journal of oceanic engineering*, *24*(2), 237-252.

Shadwick, R. E. (2005). How Tunas and Lamnid Sharks Swim: An Evolutionary Convergence: These fishes diverged millions of years ago, but selection pressures have brought them very similar biomechanical schemes for movement. *American scientist*, *93*(6), 524-531.

Sorenson, L., Santini, F., & Alfaro, M. E. (2014). The effect of habitat on modern shark diversification. *Journal of Evolutionary Biology*, *27*(8), 1536-1548.

Stanek, M. J. (2018). Characterization of a turbulent boundary layer in open channel flow using particle image velocimetry.

Stevens, J. D. (2008). The biology and ecology of the shortfin mako shark, *Isurus oxyrinchus*. *Sharks of the open ocean: biology, fisheries and conservation*, 87-94.

Suleman, A., & Crawford, C. (2008). Studies on hydrodynamic propulsion of a biomimetic tuna. *Underwater vehicles*, 459-486.

- Tamura, Y., & Takagi, T. (2009). Morphological features and functions of bluefin tuna change with growth. *Fisheries Science*, 75(3), 567-575.
- Takagi, T., Tamura, Y., & Weihs, D. (2013). Hydrodynamics and energy-saving swimming techniques of Pacific bluefin tuna. *Journal of theoretical biology*, 336, 158-172.
- Taylor, Z. J., Gurka, R., Kopp, G. A., & Liberzon, A. (2010). Long-duration time-resolved PIV to study unsteady aerodynamics. *IEEE Transactions on Instrumentation and Measurement*, 59(12), 3262-3269.
- Thomson, K. S., & Simanek, D. E. (1977). Body form and locomotion in sharks. *American Zoologist*, 17(2), 343-354.
- Triantafyllou, G. S., Triantafyllou, M. S., & Grosenbaugh, M. A. (1993). Optimal thrust development in oscillating foils with application to fish propulsion. *Journal of Fluids and Structures*, 7(2), 205-224.
- Trump, C. L., & Leggett, W. C. (1980). Optimum swimming speeds in fish: the problem of currents. *Canadian Journal of Fisheries and Aquatic Sciences*, 37(7), 1086-1092.
- Turner, V. L. (2020). Investigating Dorsal Fin Hydrodynamic Function of the Lemon Shark, *Negaprion brevirostris*.
- Tytell, E. D. (2004). The hydrodynamics of eel swimming II. Effect of swimming speed. *Journal of experimental biology*, 207(19), 3265-3279.
- Tytell, E. D. (2006). Median fin function in bluegill sunfish *Lepomis macrochirus*: streamwise vortex structure during steady swimming. *Journal of Experimental Biology*, 209(8), 1516-1534.

- Wang, T., Wen, L., Liang, J., & Wu, G. (2010). Fuzzy vorticity control of a biomimetic robotic fish using a flapping lunare tail. *Journal of Bionic Engineering*, 7(1), 56-65.
- Webb, P. W. (1978). Fast-start performance and body form in seven species of teleost fish. *Journal of experimental biology*, 74(1), 211-226.
- Webb, P. W., KostECKI, P. T., & Stevens, E. D. (1984). The effect of size and swimming speed on locomotor kinematics of rainbow trout. *Journal of Experimental Biology*, 109(1), 77-95.
- Wieneke, B. (2017). PIV anisotropic denoising using uncertainty quantification. *Experiments in Fluids*, 58(8), 1-10.
- Wilga, C. D., & Lauder, G. V. (2000). Three-dimensional kinematics and wake structure of the pectoral fins during locomotion in leopard sharks *Triakis semifasciata*. *Journal of Experimental Biology*, 203(15), 2261-2278.
- Wilga, C. D., & Lauder, G. V. (2002). Function of the heterocercal tail in sharks: quantitative wake dynamics during steady horizontal swimming and vertical maneuvering. *Journal of Experimental Biology*, 205(16), 2365-2374.
- Willert, C. E., & Gharib, M. (1991). Digital particle image velocimetry. *Experiments in fluids*, 10(4), 181-193.
- Williamson, C. H., & Roshko, A. (1988). Vortex formation in the wake of an oscillating cylinder. *Journal of fluids and structures*, 2(4), 355-381.
- Wolfgang, M. J., Anderson, J. M., Grosenbaugh, M. A., Yue, D. K., & Triantafyllou, M. S. (1999). Near-body flow dynamics in swimming fish. *Journal of Experimental Biology*, 202(17), 2303-2327.

Xia, D., Chen, W., Liu, J., Wu, Z., & Cao, Y. (2015). The three-dimensional hydrodynamics of thunniform swimming under self-propulsion. *Ocean Engineering*, *110*, 1-14.

Yang, L., & Su, Y. M. (2011). CFD simulation of flow features and vorticity structures in tuna-like swimming. *China Ocean Engineering*, *25*(1), 73-82.

Yeh, P. D., & Alexeev, A. (2016). Effect of aspect ratio in free-swimming plunging flexible plates. *Computers & Fluids*, *124*, 220-225.

Zhu, Q., Wolfgang, M. J., Yue, D. K. P., & Triantafyllou, M. S. (2002). Three-dimensional flow structures and vorticity control in fish-like swimming.

